

2022-12-01

Cryogenic Flow Boiling Heat Transfer on Additively Manufactured Liquid Rocket Engine Cooling Channels

Debra Jazmin Ortega
University of Texas at El Paso

Follow this and additional works at: https://scholarworks.utep.edu/open_etd



Part of the [Aerospace Engineering Commons](#), and the [Mechanical Engineering Commons](#)

Recommended Citation

Ortega, Debra Jazmin, "Cryogenic Flow Boiling Heat Transfer on Additively Manufactured Liquid Rocket Engine Cooling Channels" (2022). *Open Access Theses & Dissertations*. 3711.
https://scholarworks.utep.edu/open_etd/3711

This is brought to you for free and open access by ScholarWorks@UTEP. It has been accepted for inclusion in Open Access Theses & Dissertations by an authorized administrator of ScholarWorks@UTEP. For more information, please contact lweber@utep.edu.

CRYOGENIC FLOW BOILING HEAT TRANSFER ON ADDITIVELY
MANUFACTURED LIQUID ROCKET ENGINE
COOLING CHANNELS

DEBRA JAZMIN ORTEGA

Doctoral Program in Mechanical Engineering

APPROVED:

Md Mahamudur Rahman, Ph.D., Chair

Jack Chessa, Ph.D.

Joel Quintana, Ph.D.

Luis R. Contreras, Ph.D.

Stephen L. Crites, Jr., Ph.D.
Dean of the Graduate School

Copyright ©

by

Debra Jazmin Ortega

2022

Dedication

This work is dedicated to my parents, friends, colleagues and my husband for their timeless support and encouragement that they provided me in achieving this incredible milestone in my life. And most importantly, it is dedicated to God who has helped me get this far.

CRYOGENIC FLOW BOILING HEAT TRANSFER ON ADDITIVELY
MANUFACTURED LIQUID ROCKET ENGINE
COOLING CHANNELS

by

DEBRA JAZMIN ORTEGA, B.S.M.E.

DISSERTATION

Presented to the Faculty of the Graduate School of
The University of Texas at El Paso
in Partial Fulfillment
of the Requirements
for the Degree of

DOCTOR OF PHILOSOPHY

Department of Aerospace and Mechanical Engineering

THE UNIVERSITY OF TEXAS AT EL PASO

December 2022

Acknowledgements

I would like to acknowledge and thank the faculty and staff from the University of Texas at El Paso within the Mechanical Engineering department and the Aerospace Center for their aid and support. I would like to give special thanks to my fellow students Linda Hernandez, Alejandro Amador, Raul Palacios, and Gerardo Olvera. I would also like to thank all the great and caring staff from the Aerospace Center Dr. Jason Adams, Luz Bugarin, Linda Vera, Jonathan Zavala, Gloria Salas, Brenda Sanchez, and Mehnaz Rahman for their dedication and time helping me. Furthermore, I would like to thank Dr. Md Mahamudur Rahman, my mentor, who imparted his knowledge on me and guided me through this project. Lastly, I would like to thank my husband for his patience, encouragement and believing in me every step of the way.

Abstract

The enhancement of flow boiling heat transfer is critical because it can solve thermal management issues seen across all engineering and manufacturing applications. Even though advancements are being made, more studies are needed to understand the behavior of forced convective boiling further.

Currently, there are four major issues in the field of regenerative cooling of liquid rocket engines. 1. The cooling channels are typically manufactured using conventional machining, while aerospace industries are currently exploring the additive manufacturing approach. 2. The experimental critical heat flux values for cryogenic fluids are either lower or very close to the model predictions; however, the effect of roughness and the associated heat flux enhancement is not considered in the models. 3. Cryogenic flow boiling experiments are typically performed in symmetrically heated channels; however, rocket engine cooling channels experience asymmetric heating. 4. Although the chill-down experiments can measure temperature-controlled minimum film boiling, the throat section of the cooling channels experiences heat flux-controlled minimum film boiling, yet almost no literature data is available for this phenomenon.

The focus of this research is to demonstrate some potential solutions to the issues above. It will begin by investigating the flow boiling heat transfer performance of additively manufactured rocket engine cooling channels during asymmetric heating. Then, the research will identify the critical heat flux (CHF) and the minimum film boiling heat flux (MFBHF) for various channels at various pressures, degree of subcooling, flow rates, and working fluids for a cooling channel in a regeneratively-cooled rocket engine. Lastly, the research will compare the experimental results with literature models to identify the heat transfer enhancement.

The research detailed here is based on a cooling channel's flow boiling heat transfer analyses using three cooling channel hydraulic diameters – 1.8 mm, 2.3 mm, and 2.5 mm (0.07", 0.09", 0.097"), three pressures – 0.89 MPa, 1.37 MPa, and 1.58 MPa (130 psi, 200 psi, 230 psi), two degrees of sub-cooling – 0 K and 5 K, three cryogenic flow rates – 32 cm³/s, 47 cm³/s, 57 cm³/s (0.5 gpm, 0.75 gpm, and 0.9 gpm), and two different cryogenic fluids – liquid nitrogen (LN₂) and liquid methane (LCH₄).

The analyses were completed with a thermal concentrator setup known as the High Heat Flux Testing Facility (HHFTF) at the University of Texas at El Paso's Aerospace Center. The testing of the HHFTF was performed in conjunction with a methane condensing unit for the provision of LCH₄.

The results for the single-phase forced convection showed a 200% enhancement from values found in the literature, which can be attributed to the higher surface roughness due to additive manufacturing. The results for the forced convective boiling show that while using the three additively manufactured samples, the one with the greatest CHF and MFBHF was the sample with a hydraulic diameter of 1.8 mm (0.07"), seeing a positive trend with increasing mass flux with a maximum value of 14,295 kg/m²s. Another finding was that as pressure increases, CHF decreases, and as the subcooling degree increases, so does the CHF. These trends revealed that a balance between pressure and subcooling degree is needed to increase the heat flux. Finally, after comparing the results with the experimental data with the literature models, a 98% enhancement for CHF was determined. Additionally, an enhancement of 13 times the model values for MFBHF was found.

Table of Contents

Acknowledgements.....	v
Abstract.....	vi
Table of Contents.....	viii
List of Tables.....	xi
List of Figures.....	xii
Chapter 1: Introduction.....	1
1.1 Introduction.....	1
1.2 Phase Change Heat Transfer.....	4
1.3 Fundamentals of Flow Boiling.....	4
1.3.1 Subcooled Flow Boiling Regimes.....	6
1.3.2 Fluid Quality.....	6
1.3.3 Heat Transfer Coefficient.....	6
1.3.4 Departure from Nucleate Boiling.....	7
1.3.5 Critical Heat Flux.....	7
1.3.6 Minimum Film Boiling Heat Flux.....	8
1.4 UTEP Aerospace Center.....	9
1.5 Overview of Dissertation.....	9
Chapter 2: Motivations and Objectives.....	11
2.1 Motivations.....	11
2.2 Objectives and Contributions to the field.....	12
Chapter 3: Literature Review.....	14
3.1 Internal Flow Boiling.....	14
3.1.1 Nucleation.....	15
3.1.2 Bubble Growth and Departure.....	16
3.1.3 Vapor Quality.....	17
3.1.4 Departure from Nucleate Boiling and Critical Heat Flux.....	18
3.1.5 Minimum Film Boiling Heat Flux.....	19
3.2 Heat Transfer Coefficient.....	20

3.3	Boiling of Liquid Nitrogen	22
3.4	Boiling of Liquid Methane.....	23
Chapter 4: Theoretical Analysis.....		25
4.1	Single-Phase Forced Convection	25
4.2	CHF Analysis.....	26
4.3	MFBHF Analysis	29
Chapter 5: Experimental Apparatus.....		32
5.1	High Heat Flux Test Facility.....	32
5.2	Methane Condensing Unit	36
5.3	Experimental Method: Test Procedures.....	38
5.4	Data Analysis	39
5.5	Uncertainty Analysis.....	41
Chapter 6: Experimental Results		43
6.1	Single-Phase Forced Convection	43
6.2	Forced Convective Boiling	46
6.2.1	CHF/DNB Detection.....	47
6.2.2	MFBHF Detection	49
6.2.3	Results for $D_h = 2.5$ mm Channel	51
6.2.4	Results for $D_h = 2.3$ mm Channel	52
6.2.5	Results for $D_h = 1.8$ mm Channel	52
6.2.6	Effect of Mass Flux.....	53
6.2.7	Effect of Hydraulic Diameter.....	54
6.2.8	Effect of Pressure	55
6.2.9	Effect of Degree of Subcooling	56
6.2.10	Effect of Fluid	58
6.2.11	Effect of Surface Roughness.....	59
6.2.12	Comparison with Models.....	59
Chapter 7: Summary and Contributions		62
7.1	Overall Summary	62
7.2	Specific Contributions to the Field	64
7.3	Recommendations for Future Research	64

References.....	65
Appendix A – Instrumentation.....	73
Appendix B – Extra Data.....	76
Curriculum Vita	78

List of Tables

Table 4-1. Inconel 625 samples' roughness with respective manufacturing method	25
Table 5-1. Instrumentation Measurement Accuracy	42
Table 6-1. Flow boiling Test Matrix	47
Table 6-1. CHF and MFBHF results for sample Dh = 2.5 mm	51
Table 6-2. CHF and MFBHF results for sample Dh = 2.3 mm	52
Table 6-3. CHF and MFBHF results for sample Dh = 1.8 mm	52
Table 6-4. Model CHF values for all three samples at 1.37 MPa, 0 k.....	60
Table A-1. High Heat Flux Testing Facility Instrumentation.....	73

List of Figures

Figure 1-1. Liquid Bipropellant Rocket Engine with Labels.....	3
Figure 1-2. Forced Convective Boiling Stages [32, 33].	3
Figure 1-3. Variation of the heat transfer coefficient and flow regime with internal convective boiling.	5
Figure 1-4. Typical boiling curve with heat flux as a function of wall superheat temperature minus saturation temperature. [82]	8
Figure 2-1. Combustion chamber with cooling channels and metal jacket.	12
Figure 3-1. Liquid nitrogen heat transfer apparatus.....	20
Figure 3-2. Schematic diagram of experimental system: 1. Nitrogen gas cylinder 2. Liquid nitrogen tank (High pressure) 3. Vacuum chamber 4. Liquid nitrogen tank (Low Pressure) 5. Liquid tank 6. Test section 7. First heater 8. Second heater 9. Vaporizer 10. Flow rate meter 11. Vacuum pump. [19].	23
Figure 4-1. Nucleate boiling heat flux as a function of nucleate boiling temperature difference. 30	
Figure 4-2. Typical graphical solution of the minimum heat flux. $PPc = 0.071, A = 0.872$	31
Figure 5-1. High Heat Flux Testing Facility.....	32
Figure 5-2. HHFTF inner assembly composed of inlet and outlet lines, stainless steel test stand, cradle, sample, copper wafer, and a heating block (lines are frosted from cryo temperatures). ..	33
Figure 5-3. HHFTF inner assembly drawing composed of sample, copper wafer, and a heating block with thermocouples labels and placement (from top to bottom).	34
Figure 5-4. Pressure transducers for A) inlet of the system, and B) outlet of the channel.	35
Figure 5-5. Constant pressure delivery system.	35
Figure 5-6. VARIAC, variable transformer	36
Figure 5-7. MCU with liquid nitrogen dewar.	37
Figure 5-8. Methane and helium tanks.	37
Figure 5-9. Methane condensing unit with fluids and schematic to HHFTF.....	38
Figure 5-10. Instrumentation of the delivery system for the HHFTF consisting of thermocouples, pressure transducers, and a flow meter.	40
Figure 5-11. Thermocouples inside the vacuum chamber.	40
Figure 5-12. Thermocouples for the MCU.	41
Figure 6-1. Samples made from Inconel 625. A) Top view, B) Side view with grooves on the bottom.	43
Figure 6-2. Forced convection results. Heat flux as a function of $\Delta T = (T_{wall} - T_{fluid})$	44
Figure 6-3. HTC as a function of $\Delta T = (T_{wall} - T_{fluid})$	45
Figure 6-4. Pressure drop as a function of Reynolds number.....	45
Figure 6-5. Experimental Nusselt numbers plotted with NASA Rocketdyne correlation, Dittus-Boelter model, Sieder-Tate model, and Gnielinski correlation	46
Figure 6-6. Typical test section response for increasing heat flux found by VanNoord [87].....	48
Figure 6-7. Heat flux as a function of temperature different (ΔT) and temperature in K.	49
Figure 6-8. Heat flux as a function of ΔT and temperature in K.	50
Figure 6-9. Boiling Hysteresis tested up to 489 kW/m^2 with no CHF.	51
Figure 6-10. CHF as a function of mass flux for all three samples.	53
Figure 6-11. MFBHF as a function of mass flux for all three samples.	54
Figure 6-12. Effects of hydraulic diameter on CHF and MFBHF as function of mass flux.	54

Figure 6-13. Effects of pressure on CHF and MFBHF as a function of mass flux.	56
Figure 6-14. CHF and MFBHF as a function of mass flux with 0 and 5 K degree of subcooling.	57
Figure 6-15. CHF and MFBHF as a function of mass flux with the effect of combined pressure and subcooling degree.....	58
Figure 6-16. CHF and MFBHF as a function of mass flux with LCH ₄ and LN ₂ at 1.37 MPa.	59
Figure 6-17. Model CHF values and Experimental CHF values as a function of mass flux under different operating conditions.	60
Figure 6-18. Model MFBHF values and Experimental MFBHF values as a function of mass flux under different operating conditions.....	61
Figure B-1. CHF and MFBHF for sample with D _h = 1.8 mm as a function of mass flux	76
Figure B-2. CHF and MFBHF for sample with D _h = 2.3 mm as a function of mass flux	76
Figure B-3. CHF and MFBHF for sample with D _h = 2.5 mm as a function of mass flux	77

Chapter 1: Introduction

1.1 Introduction

The space industry is a fast-growing and fast-paced environment with a continuous challenge to expand the boundaries of the capabilities of technology. Amongst the different types of rocket engines, there is a very efficient engine, the regeneratively-cooled liquid rocket engine. It functions by using the fuel not just for combustion but as the coolant that flows through the cooling channels around the combustion chamber and nozzle. This process aims to cool down the engine during combustion to prevent hardware damage while reducing the time it takes for the cryogenic fluid to warm up; hence the combustion can happen with greater efficiency.

The standard rocket engine fuels used are liquid hydrogen (LH₂), rocket-grade kerosene (RP-1), and hydrazine, all with various advantages and disadvantages. The advantages of these fuels are that they provide a high specific impulse in space; the disadvantages are that some of the fuels are toxic, carcinogenic, hypergolic (such as RP-1 and hydrazine), and challenging to store, in the case of LH₂, requiring huge tanks and extremely cold temperatures. Another option for a fuel that has emerged recently is liquid methane (LCH₄) or liquid natural gas (LNG), a propellant with a storage temperature of 110 K at atmospheric pressure, 0.1 MPa (14.5 psi), in contrast to LH₂'s storage temperature of 20 K at that same pressure.

Additive manufacturing has been developing rapidly; today, it allows for different surface roughness, complicated geometries, and microstructures. Due to the difficulty of testing with LH₂, data can be collected using liquid nitrogen (LN₂) since it has similar properties, is non-flammable, and has a higher storage temperature of 109 K at 1.38 MPa (200 psi). The data required is the critical heat flux (CHF) and minimum film boiling heat flux (MFBHF) as a function of the

temperature difference between the wall superheat temperature and saturation temperature of the fluid. Rocket engines reach such high temperatures that can melt the engine, hence the desire for a higher value of CHF; better cooling allows for more tolerance for higher temperatures.

Gradl [27] did development testing with GRCop-42, performed as an improvement from GRCop-84, with high conductivity and faster build speeds. A new additive manufacturing method was also explored, blown powder-directed energy deposition with Inconel 625 and JBK-75 alloys [26]. Both nozzles had a total test time of 1,072 and 4,170 seconds, respectively, with post-inspections showing good conditions and no leaks.

The cooling channels undergo boiling as they remove the heat from the engine, but the critical area is the throat [77, 80], shown in Figure 1-1, where the engine experiences the highest heat. For this reason, channels with higher efficiency and tolerance to high heat fluxes are needed. Another form of cooling that is very well known is boundary-layer film cooling, as shown by Back et al. [4]; it experiences the same drop in heat transfer efficiency downstream of the throat.

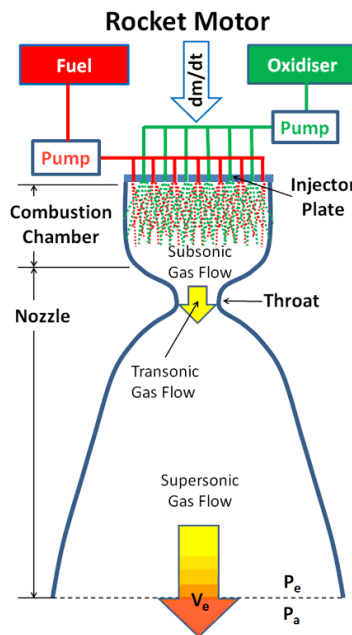


Figure 1-1. Liquid Bipropellant Rocket Engine with Labels.

As the fuel flows through the cooling channels, it undergoes forced convective boiling. The forced convective boiling stages, also known as flow boiling stages, are single-phase liquid, bubbly flow, plug flow, annular flow, mist flow, and single-phase vapor [14], as seen in Figure 1-2. The transition begins with a single-phase liquid. As the given heat flux increases, so does the temperature and individual bubbles begin to form, signifying the flow has entered bubbly flow [62, 68]. As the heat flux increases, the bubbles grow and, due to drag force, detach from the wall and flow with the liquid [16, 84]. The surface continues to increase in temperature leading the flow to plug flow, where the bubble departure increases in speed and becomes jets or columns as they get close together and rise [60, 64].

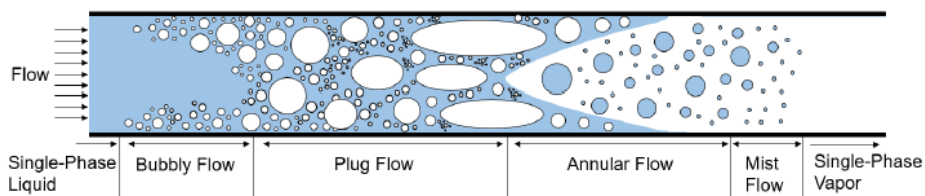


Figure 1-2. Forced Convective Boiling Stages [32, 33].

Consequently, the flow transitions to annular flow, where the quality dramatically increases as the bubbles begin to cover the solid-and-liquid interface. From this point, the flow transitions to mist flow, where a thin vapor film forms on the surface, causing a decrease in the heat transfer coefficient (HTC) and a spike in temperature, and so the flow enters the film boiling regime. The spike in temperature denotes that the critical heat flux (CHF) has been reached [1, 32, 33, 73]. From this stage, the flow becomes a single-phase vapor with a quality of 1 with the lowest value

of HTC, also known as dry out [90]. Nonetheless, more testing is needed to truly understand the behavior of the flow inside the cooling channels and how it transitions through the boiling stages to manufacture new channels with higher efficiency.

1.2 Phase Change Heat Transfer

Flow begins with a single-phase liquid, which can also be called film condensation in a closed-loop system, as Mills [68] discussed. At this stage, no heat is applied to the channel, and the liquid ideally has a quality of 0. In a horizontal tube, there is laminar film condensation. As energy, in this case in the form of heat, is introduced into the channel, the flow begins to change phases to a two-phase flow as it begins forced-convective boiling. The boiling will reach a limit in heat flux known as the CHF, and then it will enter the film boiling regime and transition to the vapor phase. Latent heat of vaporization is the energy absorbed that changes the state of a fluid from liquid to vapor. This dissertation will further discuss the stages of phase change as nucleation cavities form in the various nucleation sites of the surface and how it relates to heat flux and pressure.

1.3 Fundamentals of Flow Boiling

To properly analyze the liquid-vapor phase change inside the channel, it is essential to understand the behavior of fluids as boiling begins. The heterogeneous nucleation process is where an embryo (onset of a bubble) is formed on the solid surface at a nucleation site and is in contact with both the solid and liquid phases at the interface [14]. As heat flux increases, the bubbles grow, the quality of the fluid goes up, as seen in Figure 1-3, and the void fraction, the ratio of the amount of space the vapor occupies in the channel to the total volume of the channel, increases until it attains single-phase vapor stage.

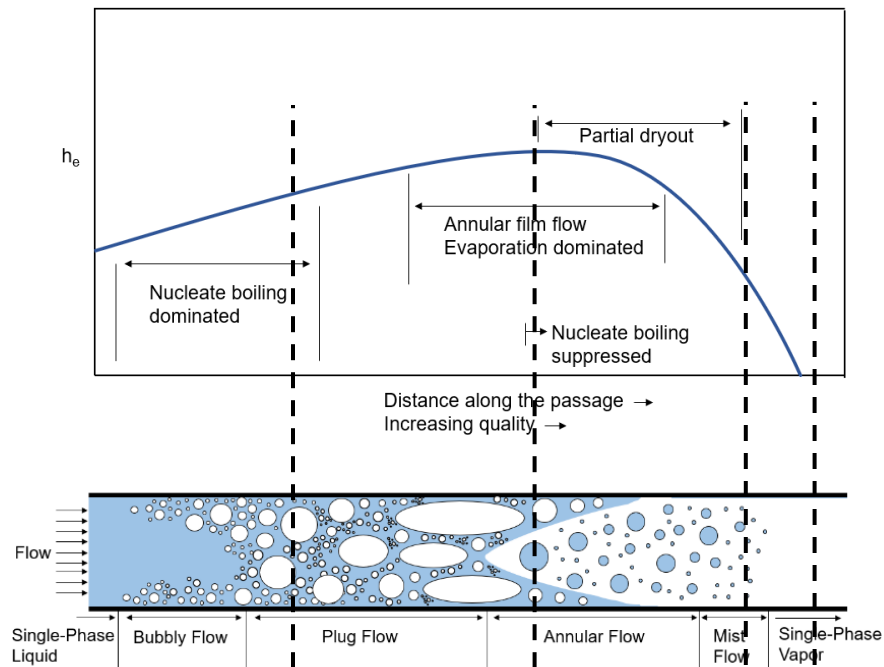


Figure 1-3. Variation of the heat transfer coefficient and flow regime with internal convective boiling.

There are six stages in the flow boiling regime: single-phase liquid, bubbly flow, plug flow, annular flow, mist flow, and single-phase vapor. Heat flux is applied as the single-phase liquid begins to flow through the channel, and bubbles begin forming at nucleation sites, causing the fluid to transition to a bubbly and plug flow. As the temperature rises, the bubbles grow in size and begin leaving the surface faster, creating tunnels, also known as columns, of bubbles as they coalesce.

At this point, as mentioned before, the fluid transitions into the annular flow, where the flow increases in vapor content, and a thin film forms on the interface, creating a partial dryout and allowing the flow to enter the film boiling regime. Consequently, the flow transitions to mist flow, where the thin film covers the entire surface; considering liquids have a higher HTC than vapors, the physical property's value drops, and the interface cannot remove the heat properly,

leading to superheating. This point is referred to as surface dryout, where the fluid becomes a single-phase vapor.

1.3.1 Subcooled Flow Boiling Regimes

Dealing with cryogenics has its challenges, such as keeping the fluid as a fully saturated liquid. The metal tubing, along with the channel sample, begins at an ambient temperature of about 300 K, which means a chill down of the lines is needed for the cryogenic to remain liquid. The longer the chill down runs, the more opportunity the fluid has to become subcooled. The colder the temperature, the more subcooled the fluid is at that specific pressure. This flow boiling regime gives the sample a higher HTC since it gives the fluid more time to be liquid, absorb the heat, and cool down the surface. Celata and Chen [15, 16] discuss in more detail the available data for subcooled flow boiling CHF, as well as correlations and several references for this regime. Celata claims that CHF is a local phenomenon under subcooled and low-quality conditions.

1.3.2 Fluid Quality

At the beginning of the test, the fluid (LN_2/LCH_4) begins as a liquid with an ideal quality of 0, assuming a fully saturated fluid. As heat is introduced to the channel, the quality begins to increment as the fluid goes through the boiling stages of bubbly and plug until it reaches the film boiling regime during the annular stage, reaching a higher quality closer to one. Finally, once the flow reaches the mist flow stage, the quality is 1, or 100%, and the flow is a single-phase vapor.

1.3.3 Heat Transfer Coefficient

The HTC is the heat flux divided by ΔT of the superheat wall and saturation temperature. During the boiling stage of plug flow, it can be seen that that is where the highest values of HTC are since it removes the maximum heat from the sample; further explanation of the

stages of boiling can be found in Section 3.2. As the boiling increases due to the increase in energy to the channel, the bubbles grow in size and coalesce with each other forming columns that rise, which slowly decreases the HTC values, as it correlates with heat flux and working pressure, as noted by Zhang et al. [89]. The lowest value theoretically is found when the critical heat flux occurs since a vapor film covers the interface between the liquid and the surface, decreasing the heat transfer efficiency.

1.3.4 Departure from Nucleate Boiling

The terms CHF and departure from nucleate boiling (DNB) are both used to refer to the point in the convective boiling when the wall temperature rises, and the HTC decreases. The CHF term will be covered in the next section. As defined by Carey [14], the DNB occurs during subcooled conditions of the bulk flow with low qualities. It depicts the change in the boiling mechanism from nucleate to film boiling, in other words, the transition between the plug and annular flow. This term is typically used when the flow has a lower quality value. It will be further discussed in Section 3.1.4.

1.3.5 Critical Heat Flux

Every material has a specific thermal conductivity, and the higher the value the higher the limit for the heat transfer properties. Moreover, the CHF has been reached once the sample reaches superheat temperatures and the HTC drops to its lowest point. As defined by Carey [14], the CHF, or dryout, occurs during moderate to high qualities as the flow is in the annular boiling stage and the liquid film on the surface dries out.

The typical boiling curve, shown in Figure 1-4, begins with nucleate boiling from point A to point B; as the bubbles continue to grow in size, they reach a point where the bubbles grow so

much they begin to completely cover the surface, cause a thin vapor film, as has been discussed in the previous sections. At this point the flow has entered a film boiling regime and the CHF has been reached. The CHF is depicted by a spike in temperature of 50 to 100 degrees, going from point B to point C, where, in theory, the heat flux remains constant while the temperature difference rises [82]. Boiling burnout follows this phenomenon, which characterizes when failure happens at the passage wall due to overheating and melting [14].

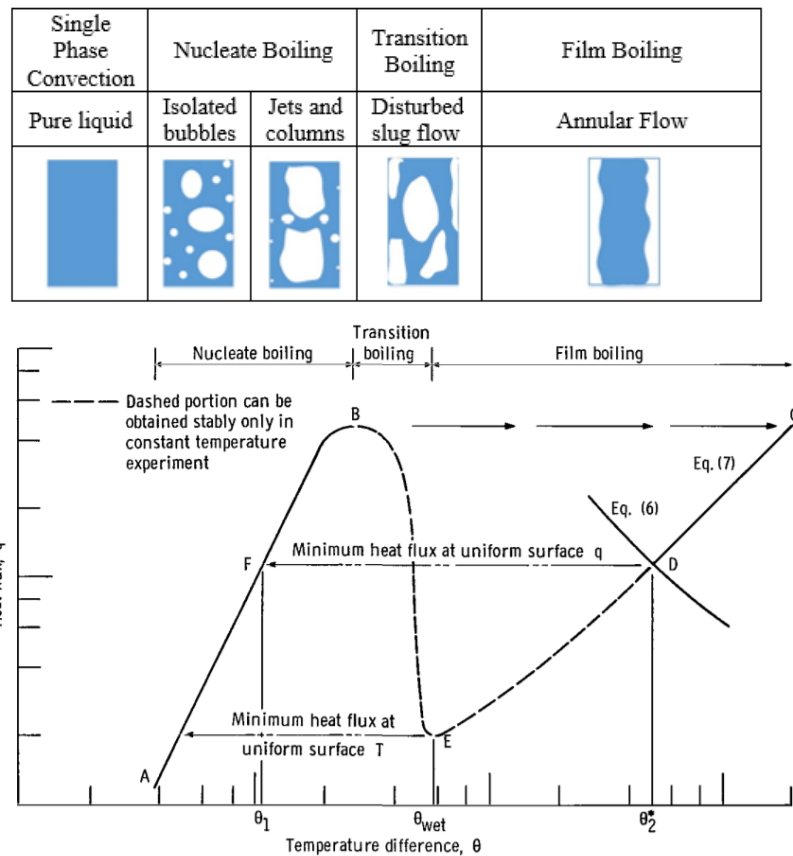


Figure 1-4. Typical boiling curve with heat flux as a function of wall superheat temperature minus saturation temperature. [82]

1.3.6 Minimum Film Boiling Heat Flux

Two types of systems can be used to investigate the MFBHF: temperature-controlled and heat flux-controlled. In a temperature-controlled experiment, the temperature is kept constant, and

the curve goes from point B to E and then to C on the graph in Figure 1-4 [81]. The experiments found in this dissertation were performed using the High Heat Flux Testing Facility (HHFTF) [31, 32, 85, 86], a heat-flux controlled system where the heat flux follows the pattern from point B to C, where the cooling channel reaches CHF. As the heat going into the system is reduced, it declines to point D. Point E is the MFBHF for a temperature-controlled system, but for a heat flux-controlled system, it is physically unable to reach that point. Hence, as the heat is slowly reduced, the lowest point it can reach is point D, and from there, it transitions to point F. From point D to point F, a significant descent in temperature difference can be seen as the heat flux remains constant. For a temperature-controlled system, the boiling stages follow the order of A to B to E to C. This topic will be further discussed in Section 3.1.5.

1.4 UTEP Aerospace Center

The Aerospace Center is under the direction of Dr. Ahsan Choudhuri with several faculty, staff, and graduate and undergraduate students. Its goal is to promote research and higher education in aerospace and energy technologies. A grant was awarded to the Aerospace Center by NASA Marshall Space Flight Center to complete the testing necessary for this project at the Technology Research and Innovation Acceleration Park (tRAIC) located in Fabens, TX.

In addition, the Center has several partners in the Federal, Industrial, and Academia realm, including the National Aeronautics and Space Administration (NASA), the U.S. Department of Energy (DoE), Lockheed Martin, Blue Origin, and Princeton University, to name a few.

1.5 Overview of Dissertation

This dissertation is comprised of seven chapters. Chapter 1, as noted, consisted of an introduction to the world of regenerative rocket engines, phase change heat transfer, the

fundamentals of flow boiling, and more detail about the sub-cooled flow boiling regimes, fluid quality, heat transfer coefficient, CHF, and MFBHF. It also developed on the Aerospace Center, its goal and connections.

Chapter 2 focuses on the motivation and objectives of this project. Chapter 3 covers an extensive review of literature on boiling in channels of various shapes, vapor quality, heat transfer coefficient (HTC), and liquid nitrogen and methane behavior. Chapter 4 will go over the theoretical analysis of the CHF and MFBHF, including equations and the reasoning behind their usage of them. Then the experimental apparatus will be described in Chapter 5 with images of the High Heat Flux Testing Facility (HHFTF) and the Methane Condensing Unit (MCU), along with how the testing was done and the data analysis. Chapter 6 will cover the experimental results, dive into how the data was interpreted, explain the values, and analyze the effects of mass flux, hydraulic diameter, pressure, degree of subcooling, fluid, and surface roughness that caused an effect on the results. Lastly, Chapter 7 will summarize the whole project, how it impacts the field, and its contributions.

Chapter 2: Motivations and Objectives

2.1 Motivations

There are four major issues in the field of regenerative cooling, starting with the manufacturing of cooling channels. First, the cooling channels are typically manufactured conventionally, but now the aerospace industry wants to move forward with additive manufacturing, or 3D printing, in the hopes of reducing costs and manufacturing time. The second issue is that in the literature analyzed herein, the experimental CHF values for cryogenic fluids tend to be lower or similar to the model predictions. After further analysis, it was discovered that the effect of surface roughness and its heat flux enhancement is not considered in any of the models. Thirdly, the cryogenic flow boiling experiments are typically rendered with symmetrically heated channels, although rocket engine cooling channels experience asymmetric heating from the bottom of the channels.

Lastly, the fourth issue is that even though the chill-down experiments are able to measure temperature-controlled MFBHF, the throat section of the engine experiences a heat flux-controlled MFBHF, which needs to be significantly improved in the literature since almost no literature was found on this subject. This research's primary purpose focuses on demonstrating potential solutions to each of these issues. Furthermore, this project was funded and motivated by NASA Marshall Space Flight Center (MSFC) with rocket conditions with the most concern of around 8.2 MW/m^2 to 16.4 MW/m^2 ($5 \text{ BTU/in}^2\text{s}$ to $10 \text{ BTU/in}^2\text{s}$). The testing was designed to use additive manufacturing to include greater surface roughness to enhance boiling, hence heat transfer, inside the channel and compare the results with the models.

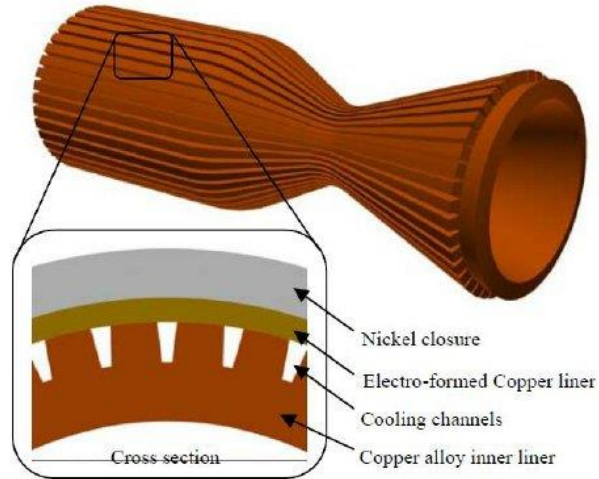


Figure 2-1. Combustion chamber with cooling channels and metal jacket.

2.2 Objectives and Contributions to the field

This dissertation investigates the stages of flow boiling using a system resembling a calorimeter, the HHFTF, to gather a fundamental understanding of the operating conditions to reach CHF and MFBHF. The main three objectives for this project are stated below.

The first objective is to investigate the flow boiling heat transfer performance of additively manufactured rocket engine cooling channels during asymmetric heating with the heat coming from the bottom.

The second objective is to identify the CHF and MFBHF for three different channels at various conditions using cryogenics, specifically LN_2 and LCH_4 . The operating conditions consist of pressures of 0.89 MPa (130 psi), 1.38 MPa (200 psi), and 1.59 MPa (230 psi) with their respective saturation temperatures; degrees of subcooling of 0 K and 5 K; and flow rates of $32 \text{ cm}^3/\text{s}$ (0.5 gpm), $47 \text{ cm}^3/\text{s}$ (0.75 gpm), and $57 \text{ cm}^3/\text{s}$ (0.9 gpm). The wall's surface roughness, although it wasn't analyzed for a specific value, was assumed to increase heat transfer based on data from other additively manufactured samples found in Section 6.1. The tests were performed

on three different samples additively manufactured with GRCop-42, a copper alloy manufactured by NASA MSFC, with hydraulic diameters of 1.8 mm (0.07") (height-to-width aspect ratio of 1:1), 2.3 mm (0.09") (aspect ratio of 1:1), and 2.5 mm (0.097") (aspect ratio of 2.3:1.8).

The third and last objective is to compare the experimental results with the literature models to identify the heat transfer enhancement, equations can be found in Section 4.

Chapter 3: Literature Review

3.1 Internal Flow Boiling

Internal flow boiling takes place inside a channel of various shapes and dimensions as it is heated. It is used in various types of engines, such as vehicle engines in the form of radiators which are used to cool down the engine through conduction and convection [22].

In the “Evolution of Microchannel Flow Passages”, Mehendale et al. [67] talk about classification through the dimensions of the channel, such as microchannels (1-100 μm), mesochannels (100 μm to 1 mm), compact passages (1 mm to 6 mm), and conventional passages (above 6 mm). On the other hand, Kandlikar [35, 37] classifies the channel based on the flow considerations, such as molecular channels (hydraulic diameter below 0.1 μm), transitional nanochannels (0.1-1 μm), transitional microchannels (1-10 μm), microchannels (10-200 μm), minichannels (hydraulic diameter (D_h) of 200 μm -3 mm), and conventional channels (3 mm or larger). The samples that this project focuses on include the classification of compact passages with respect to dimensions with the longest length of 4 mm and minichannels with a hydraulic diameter of 2.5 mm. Kudo [52] experimented on horizontal minichannels using R134a with a D_h of 0.81 and 0.64 mm, and a length of 852 mm and obtained a heat flux of 2 to 10 kW/m^2 for boiling. While Ong [71] acknowledges the issue of not having a congruent classification of channels and seeks to improve the flow pattern map through a two-phase flow experiment. In a future project, the channels will be in the category of micro-channels and transitional micro- and nanochannels.

A study was done by Liu, X [63] on flow boiling with LN_2 under different operating conditions to analyze how the departure from nucleate boiling type CHF and the dry-out type CHF transfer heat differently due to the different vapor quality. In addition, a synthesized literature

review was done along with other studies [9, 11, 12, 83] to analyze results for flow boiling inside micro-scale channels of various shapes and dimensions using fluids R245fa, R134a, water, and several others.

Another factor to consider is the pressure drop. Authors Lazarek and Black [53] use the Blasius equation to properly calculate the pressure drop due to friction, spatial acceleration, and bend hydraulic loss. Additionally, Chen [19] experimentally proved that pressure drop increases with a higher mass flux and heat flux, but it decreases with an increasing inlet pressure. Bertsch [10] did a correlation of the heat transfer of flow boiling for 14 different literature papers with 12 different fluids, with the findings of a critical heat flux ranging from 4.4 to 1,150 kW/m². Bertsch also observed that the data had the local heat transfer as a function of vapor quality and mass flux, adding to the wall heat flux, as well as how HTC decreased with the increase of quality, “convective evaporation”, which is paralleled with the results herein.

3.1.1 Nucleation

A fluid has three stages, solid, liquid, and vapor. This section focuses on what happens between the liquid and vapor stages. Nucleation begins in a cavity, a nucleation site, which is an imperfection on a surface that allows the bubble to form more easily. There are four types of cavities, completely liquid, completely gas/trapped gas, both liquid and gas, and neither liquid nor gas. Because the fluid is a mixture of liquid and gas, it is natural to have instabilities inside the channels, which was further studied [12, 13, 61, 65, 74] in microchannels.

The research done by Akbar et al. [2] investigates two-phase flow regimes in circular microchannels, and data is used to develop the Weber number-based regime map to section off the types of boiling phases. The Weber equation is discussed further in Chapter 4. The phases are the surface tension-dominated region (bubbly, plug, and slug stage), inertia-dominated zone 1

(annular), inertia-dominated zone 2 (dispersed/mist flow), and transition zone, which goes into a superheated flow.

Furthermore, Liu, D. [62] investigated the onset of nucleate boiling in a microchannel at 275 by 636 microns. A high-speed imaging system captured the onset and a model was done to predict the heat flux and bubble size as it first began. Their models aligned well with the experimental data.

3.1.2 Bubble Growth and Departure

As heat increases, so does the size of the nucleation or bubble. Once it grows enough, the bubble departs from the surface, breaking the surface tension. Ong [70] investigated bubble departure as it is difficult to know the diameters of the bubbles when they leave the surface, which also affects pool boiling. Bogojevic et al. [12] performed an investigation to analyze bubble dynamics and what effect it has on boiling instabilities. Evaporation is the principal heat transfer mechanism, and as expected, the amount of liquid on the surface decreases as the heat flux increases.

Researchers are trying to understand instability and the two-phase flow oscillation phenomena in flow boiling as it increases in quality. An investigation was done on the onset of nucleate boiling and the onset of flow instability, concluding that it primarily depends on the heat flux for bulk saturation [13, 34, 46, 79, 84].

Lee, Jae [55] investigates the difference in bubble nucleation between micro- and macro-channels with the conclusion that the inception of the bubble is similar for both, but once it comes to the growth rate, detaching, and expansion of the bubble, they differ greatly. The determining factor for the bubble growth and the type of flow derived from it is the wall superheat temperature.

3.1.3 Vapor Quality

Vapor quality is defined as the mass fraction of the total mass that is in the vapor phase in a liquid/vapor mixture. At a value of 0, the fluid is a fully saturated liquid, and as the fluid heats up, the quality value goes up; at a value of 1, the fluid is superheated, in other words, fully vapor. In internal two-phase flows, the vapor and liquid are in motion together inside the channel, hence why it is more complicated to analyze [14].

Vapor quality affects heat transfer and, consequentially, the CHF. Researchers have discovered that, with lower quality values, the limiting heat flux occurs at the departure from nucleate boiling when the fluid is a two-phase flow, as the surface begins to be fully covered by a thin vapor film. Bertsch [11] found that the vapor quality affects the heat transfer coefficient, and with a higher quality value, the limiting heat flux increases up to the CHF, also referred to as dryout.

Further research on vapor quality was done by Kharangate [47, 48], Lee [56, 57, 58], and Mishima [69], who did an investigation on two-phase flows in circular mini tubes. Kandlikar [38] developed a correlation to predict saturated flow boiling HTC's inside horizontal and vertical tubes, which he confirmed by analyzing 24 experiments with ten different fluids.

Additionally, Kim and Mudawar [49] studied the development of a correlation for the dryout incidence quality by analyzing a database of 997 quality points using 13 different fluids from 26 different sources. Their findings showed that when some correlations were applied to many different fluids and operating conditions, they yielded poor results and needed to be divided by fluid categories. Therefore, they proposed a new correlation, shown below, where q''_h is the effective heat flux averaged over the heated perimeter of the channel, P_H is the heated perimeter of the channel, and P_F is the wetted perimeter of the channel.

$$x_{di} = 1.4We_{fo}^{0.03}P_R^{0.08} - 15.0\left(Bo\frac{P_H}{P_F}\right)^{0.15}Ca^{0.35}\left(\frac{\rho_g}{\rho_f}\right)^{0.06}$$

3.1.4 Departure from Nucleate Boiling and Critical Heat Flux

The departure from nucleate boiling and critical heat flux are the same concept, where the flow transitions from annular flow to mist flow and finally to fully superheated. The difference lies in the quality of the fluid. There are two types of CHF, the departure from nucleate boiling (DNB) and the liquid film dryout, as explained by Cheng [20], Ong [70], and Liu [64]. This literature also talks about the effects of DNB and how it requires low quality.

Han Lee and Sang Lee [54] used refrigerant R113 to propose a new correlation for HTC during flow boiling using rectangular channels with low aspect ratios. The Lockhart-Martinelli correlation predicted the frictional pressure drop during flow boiling.

Kandlikar [39] defined the following ranges of hydraulic diameters D_h that are attributed to different channels, such as conventional channels: $D_h > 3$ mm, minichannels: $D_h = 200 \mu\text{m}$ –3 mm, and microchannels: $D_h = 10 \mu\text{m}$ –200 μm . According to this definition, the distinction between small and conventional-size channels is 3 mm. Liu [64] also offers a review of many sources about CHF models based on experiments and modeling to validate the effectiveness of the given models. Lazarek [53] also used the same method of slowly increasing heat until dryout occurred in the wall.

Agostini et al. [1] performed tests with multi channels with CHF values on the bottom wall of 219 to 522 kW/m² and found that, unlike the saturation temperature and inlet subcooling which had a negligible change on the CHF, mass velocity had the most effect on CHF as it increased. The data obtained an absolute error of about 9%.

Additionally, Chen [19] used dielectric fluid to go through microchannels of a heat sink to cool down a PCB, with heat fluxes exceeding 542, 673, and 730 kW/m², respectively, for flow rates of 35, 47, and 60 ml/min. It can be seen that, at this point, the heat transfer coefficient decreases because of the partial dryout on the surface.

Hartwig [30] did research under the NASA New Glenn Center to analyze the prediction of two-phase flow boiling and heat transfer for the use of cryogenic fluids. With their analysis using SINDA/FLUINT and GFSSP (Generalized Fluid Simulation System Program) for 214 CHF data points and 29,367 HTC data points, the correlations proved to have a high level of error for cryogenics over room temperature fluids. They concluded that different correlations need to be used when using cryogenic versus any other fluid. Klimenko [51] also attempted to make a correlation dependent on the boiling number that was accurate for cryogenics.

3.1.5 Minimum Film Boiling Heat Flux

The phenomenon of the MFBHF, also known as the Leidenfrost point, occurs when a fluid transitions from having a thin film layer on the surface to nucleate boiling, as discussed in Section 1.3.4. Two different methods can reach this point: temperature-controlled and heat flux-controlled. This research focuses on the heat flux-controlled method since we can control the voltage and power going into the system using a variable transformer. Unfortunately, there is little literature on this topic, except for the paper by Simon et al. [81]. He performed experiments with the setup shown in Figure 3-1, with a vertical sample.

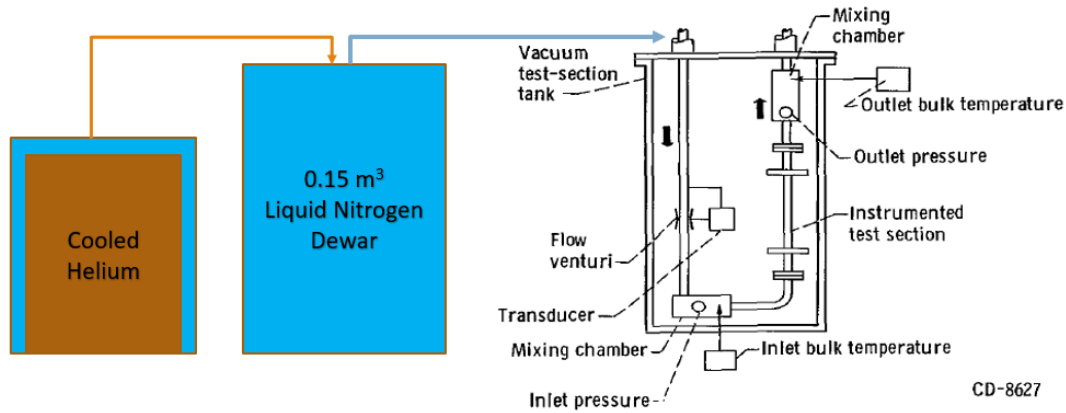


Figure 3-1. Liquid nitrogen heat transfer apparatus.

Simon focuses on studying MFBHF with liquid nitrogen in a vertical, electrically heated tube. The results showed that properly calculating the wetting temperature difference is very important and that the MFBHF is higher at greater velocities. As part of the procedure, the test section was heated before the flow of liquid nitrogen. Once everything is pre-heated, and the respective lines are chilled in, the LN₂ flows through the test section. Once film boiling was reached, the power level was decreased, keeping the pressure and flow rate constant. During the decrease of power, 1.5 minutes was given between each change to observe when nucleate boiling would begin replacing film boiling.

3.2 Heat Transfer Coefficient

The HTC can be defined as the convective heat transfer between a fluid and a surface (i.e., interface). There are several factors affecting its effectiveness. Lee and Saitoh [59, 78] had the local HTC as a function of vapor quality and mass flux, plus the wall heat flux, as was noted by Chen [17]. The results showed that the HTC decreased with the increase in quality, implying convective evaporation.

On the other hand, Lazarek and Black [53] determined that the HTC depended on the heat flux but not the vapor quality, which differs completely from Chen’s findings. Nonetheless, they also mentioned that the main heat transfer stage happens during nucleate boiling, which Chen sees as well. It is noted by Bertsch [10] that recent literature is still being developed to gather more data to overcome the mean absolute error (MAE) of 40% on testing for micro- and minichannels, which can be attributed to the low amount of tests being performed. Chen also talks about how nucleate boiling, convective evaporation, and dryout can all happen simultaneously at different locations along the channel. Bao and Qi et al. [7, 75, 76] found conditions where the surface tension decreases with the increase in pressure, meaning the increase in pressure improves the HTC, which was the reasoning behind increasing the pressure as much as possible for the HHFTF.

Kim and Mudawar [50] analyzed a total of 2378 data points from 16 different papers, with various fluids with a new method of predicting two-phase frictional pressure drop, which helps have a lower MAE of 17.2%, equation shown below in Eqn. (1) and more accuracy over a broad range of parameters. They take into account both a three-wall heated section and a one-wall heated section, similar to the calculations performed for the HHFTF.

$$MAE = \frac{1}{N} \sum_1^N \frac{\left| \frac{dP}{dz_{F,pred}} - \frac{dP}{dz_{F,exp}} \right|}{\frac{dP}{dz_{F,exp}}} \times 100\% \quad (1)$$

Balasubramanian et al. [5, 6] performed experiments using copper rectangular and stepped fin microchannels with a surface roughness of 2 μm using water as the working fluid. Employing the Taitel-Dukler flow regime map through a plot, a heat flux of 1.4 MW/m^2 was obtained, confirming that thin film evaporation is a critical stage for heat transfer. It was also discovered that the annular flow stage provides a stable flow boiling development. The work by Kandlikar [36, 37] covers the correlations and trends.

Chen, T. [18] backs the findings found in this paper, stating that if the heat flux is low, the HTC increases as the heat flux does, but if the heat flux values are high, then the HTC decreases as it continues to increase using FC-77 a perfluorinated dielectric liquid, as they flow through 24 microchannels in a silicon substrate.

Author Lee, S. [60], investigated the pressure drop and heat transfer characteristics under flow boiling using a micro-channel; the model assessed the turbulence effects.

3.3 Boiling of Liquid Nitrogen

Boiling of liquid nitrogen consists of adding heat to the liquid to boil off with the potential to take a great deal of energy as it continues to flow through. In this case, the boiling happens inside a channel in order to cool down the walls. LN₂ has a saturation temperature of -163 °C at 1.38 MPa, and the higher the pressure, the warmer the temperature is and the longer it will remain liquid. An et al. [3] conducted an investigation of liquid nitrogen on a stainless steel minichannel with three different mass fluxes of 1260, 1800, and 2050 kg/m²s, yielding a heat flux range of 8.9 to 94.4 kW/m². Their findings consisted of very low heat flux values because the thermal conductivity of this material is 15 W/mK. The thermal conductivity is why this investigation that uses the HHFTF uses Inconel 625 and a copper alloy.

Chen, X. [19] performed an experiment with two-phase liquid nitrogen under flow boiling conditions using electrical heating wires, shown in Figure 3-2, that provide heat all around the test sample with a pressure ranging from 0.17 to 0.35 MPa and a mass flux of 140 to 330 kg/m²s. Their finding concluded that the pressure drop correlates to the mass flux and heat flux but has an inverse relationship with inlet pressure. Several correlations were used to compare the pressure drop of the two-phase flow.

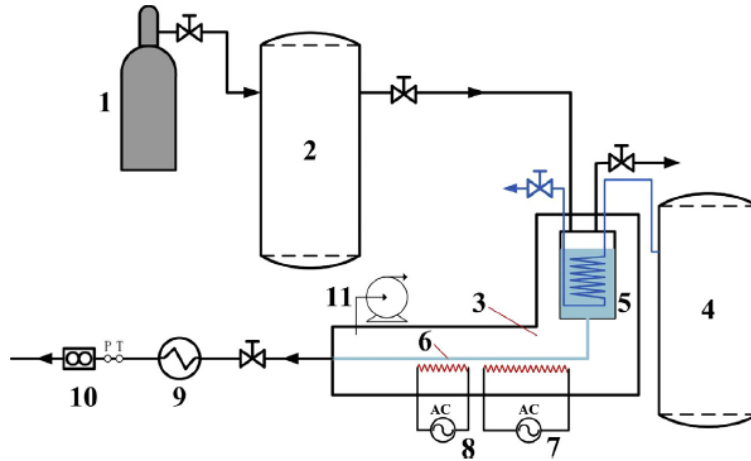


Figure 3-2. Schematic diagram of experimental system: 1. Nitrogen gas cylinder 2. Liquid nitrogen tank (High pressure) 3. Vacuum chamber 4. Liquid nitrogen tank (Low Pressure) 5. Liquid tank 6. Test section 7. First heater 8. Second heater 9. Vaporizer 10. Flow rate meter 11. Vacuum pump. [19].

Darr [21] used MATLAB to run 1D numerical simulations for a vertical stainless steel tube using liquid nitrogen data, which was compared to 55 experimental tests. Kandlikar [38] performed several tests as well using ten different fluids on vertical channels. It was concluded that different correlations could be used at specific local conditions to increase the accuracy of the data analysis for the various heat transfer coefficient correlations. Fu [24] also experimented with liquid nitrogen in vertical minichannels and used a high-speed digital camera. The results found were that the transition boundary from the bubbly flow to slug flow shifted to higher velocity, whereas from churn to annular flow, it shifted to lower velocity. Fu also noted that a negative pressure drop was seen, which was caused by severe pressure oscillation due to evaporation.

3.4 Boiling of Liquid Methane

Liquid methane has a saturation temperature of $-116\text{ }^{\circ}\text{C}$ at 1.38 MPa . When comparing it to LN_2 , LCH_4 more manageable to contain as a liquid. Something to consider for LCH_4 is that it is flammable with a lower explosive limit (LEL) of 5 and an upper explosive limit (UEL) of 17. If

the concentration of the fluid in the air is below the LEL, there is not enough fluid for a spark to ignite it. If the concentration of the fluid in the air is above the UEL, the gas is too noble and loses its flammability.

Trejo [85, 86] investigated transient heat transfer of LCH₄ using the HHFTF as well with a sample with dimensions of 1.8 mm x 1.8 mm. His goal was also to analyze cooling channels for a rocket engine and obtain a heat flux ranging from 1.19 to 3.80 MW/m². He observed that film boiling may have occurred with the combination of higher heat fluxes and a lower Reynolds number.

Gong [25] performed testing with methane where, as the heat flux rises, more nucleation sites get activated, leading to an acceleration of bubble growth and departure.

The research done by Haemisch [29] studied methane heat transfer deterioration in the cooling channels of a rocket engine at the critical point of the throat, the hottest point. The equation shown below was used as an indicator of whether heat transfer deterioration had or had not occurred, where $(\dot{q}_w/G)_{tr}$ is the ratio of heat flux and mass flow per area with [J/kg] units, and P_{in} is the inlet pressure is Pa.

$$\left(\frac{\dot{q}_w}{G}\right)_{tr} = 43.2 \cdot 10^{-6} \cdot P_{in} + 31.4$$

Chapter 4: Theoretical Analysis

4.1 Single-Phase Forced Convection

Tests were performed on four samples made from Inconel 625 with a cross-section of 3.2 x 3.2 mm, with various surface roughness. The roughness, channel relative roughness, and manufacturing methods are shown in Table 4-1 [31].

TABLE 4-1. INCONEL 625 SAMPLES' ROUGHNESS WITH RESPECTIVE MANUFACTURING METHOD

Sample Name	Manufacturing Method	Roughness (Ra) (μm)	ε (%)
INCO 12.5 μm	Additive	12.5	0.400
INCO 6.4 μm	Traditional	6.4	0.200
INCO 3.2 μm	Traditional	3.2	0.100
INCO 0.8 μm	Traditional	0.8	0.025

Correlations for the Nusselt number for single-phase forced convection were obtained from literature and are shown below, starting with the NASA Rocketdyne correlation in Eqn. (2). This correlation uses: the Reynolds number, which is the ratio between inertial and viscous forces; the Prandtl number is the ratio of momentum diffusivity to thermal diffusivity, which is the speed of heat transfer by conduction concerning flow rate and temperature change; and the ratio of the bulk temperature and the wall temperature.

$$Nu = Re^{0.8} Pr^{0.4} \left(\frac{T_{bulk}}{T_{wall}} \right)^{0.45} \quad (2)$$

Dittus-Boelter model can be seen in Eqn. (3). This correlation also uses the Re number and the Pr number, with different exponents pertaining to the focus of the dimensionless number.

$$Nu = 0.023 Re_D^{\frac{4}{5}} Pr^n \quad (3)$$

Sieder-Tate model can be seen in Eqn. (4). Besides using the Re and Pr numbers, it also considers the ratio of the viscosity of the fluid at bulk temperature and at the surface temperature.

$$Nu = 0.27Re_D^{\frac{4}{5}}Pr^{\frac{1}{3}}\left(\frac{\mu}{\mu_s}\right)^{0.14} \quad (4)$$

Gnielinski correlation can be seen in Eqn. (5). This correlation considers the Darcy friction factor, which can be obtained from a Moody chart; it changes with the Re number. The comparison between the results and the correlations will be covered in Section 6.1.

$$Nu = \frac{(f/8)(Re_D - 1000)Pr}{1 + 12.7(f/8)^{\frac{1}{2}}\left(Pr^{\frac{2}{3}} - 1\right)} \quad (5)$$

4.2 CHF Analysis

The correlation by Katto and Ohno [45] was used to theoretically analyze the critical heat flux inside the channels, which is one of the most applicable correlations in vertical uniformly heated tubes. Starting with Eqn. (6), further discussed by Chen, S. [17], the variable We_K is the Weber dimensionless number that compares the inertial force to the surface tension, G is the mass flux in $\text{kg}/\text{m}^2\text{s}$, L is the length of the heated section in m, sigma (σ) is the surface tension in N/m, and ρ_l (ρ_l) is the liquid density in kg/m^3 . For Eqn. (7) gamma (γ) is the vapor-liquid density ratio, and ρ_v (ρ_v) is the vapor density in kg/m^3 . These equations will be used in the calculations to follow.

$$We_K = \frac{G^2L}{\sigma\rho_l} \quad (6)$$

$$\gamma = \frac{\rho_v}{\rho_l} \quad (7)$$

The main CHF, q''_{CHF} , formula can be seen in Eqn. (8) where K_K is the inlet subcooling parameter, $\hat{h}_{l,sat} - \hat{h}_{in}$ is the inlet subcooling enthalpy in J/kg, and h_{lv} is the latent heat of evaporation enthalpy in J/kg.

$$q''_{CHF} = q''_{co} \left(1 + K_K \frac{\hat{h}_{l,sat} - \hat{h}_{in}}{h_{lv}} \right) \quad (8)$$

In order to find the appropriate basic CHF, q''_{co} , and K_K values, the following correlations were used. In these equations, D is the internal diameter of the tube, and C_K is a dimensionless parameter empirically determined in previous papers written by Katto [41, 42, 43, 44] seen in Eqn. (12) through Eqn. (14). Eqn. (9) through Eqn. (13) shows five possible values for q''_{co} , just as Eqn. (14) through Eqn. (16) shows three possible values for K_K .

$$q''_{co1} = C_K G h_{lv} W e_K^{-0.043} \left(\frac{L}{D} \right)^{-1} \quad (9)$$

$$q''_{co2} = 0.10 G h_{lv} \gamma^{0.133} W e_K^{-\frac{1}{3}} \left[\frac{1}{1 + 0.0031 \left(\frac{L}{D} \right)} \right] \quad (10)$$

$$q''_{co3} = 0.098 G h_{lv} \gamma^{0.133} W e_K^{-0.433} \left[\frac{\left(\frac{L}{D} \right)^{0.27}}{1 + 0.0031 \left(\frac{L}{D} \right)} \right] \quad (11)$$

$$q''_{co4} = 0.0384 G h_{lv} \gamma^{0.6} W e_K^{-0.173} \left(\frac{1}{1 + 0.28 W e_K^{-0.233} \left(\frac{L}{D} \right)} \right) \quad (12)$$

$$q''_{co5} = 0.234 G h_{lv} \gamma^{0.513} W e_K^{-0.433} \left(\frac{\frac{L}{D}^{0.27}}{1 + 0.0031 \frac{L}{D}} \right) \quad (13)$$

$$K_{K1} = \frac{1.043}{4 C_K W e_K^{-0.043}} \quad (14)$$

$$K_{K2} = \left(\frac{5}{6}\right) \frac{0.0124 + \frac{D}{L}}{\gamma^{0.133} We_K^{-\frac{1}{3}}} \quad (15)$$

$$K_{K3} = (1.12) \frac{1.152 We_K^{-0.233} + \frac{D}{L}}{\gamma^{0.6} We_K^{-0.173}} \quad (16)$$

The C_K value depends on the ratio between the length of the heated section of the channel and the hydraulic diameter, with three different possible values shown below.

$$\frac{L}{D} < 50: \quad C_K = 0.25 \quad (17)$$

$$50 \leq \frac{L}{D} < 150: \quad C_K = 0.25 + 0.0009 \left[\left(\frac{L}{D} \right) - 50 \right] \quad (18)$$

$$\frac{L}{D} > 150: \quad C_K = 0.34 \quad (19)$$

Only one value can be used for q''_{co} , so once all the correct values have been obtained for Eqn. (9) through Eqn. (13) the process of selecting which is the proper value can be seen in the correlations below. Eqn. (20) can be used when the ratio of liquid density to vapor density, gamma γ , is below 0.15, and Eqn. (21) can be used when the ratio is over or equal to 0.15.

For $\gamma < 0.15$ (20)

$$q''_{co1} < q''_{co2}: \quad q''_{co} = q''_{co1}$$

$$q''_{co1} \geq q''_{co2}: \quad q''_{co} = \text{the smaller of } \{q''_{co2}, q''_{co3}\}$$

$$K_K = \text{the larger of } \{K_{k1}, K_{k2}\}$$

For $\gamma \geq 0.15$ (21)

$$q''_{co1} < q''_{co5}: \quad q''_{co} = q''_{co1}$$

$$q''_{co1} \geq q''_{co5}: \quad q''_{co} = \text{the larger of } \{q''_{co4}, q''_{co5}\}$$

$$K_{K1} > K_{K2}: \quad K_K = K_{K1}$$

$$K_{K1} \leq K_{K2}: \quad K_K = \text{the smaller of } \{K_{K2}, K_{K3}\}$$

As shown in Eqn. (22), the values for a vertical tube need to be calculated before solving the horizontal values, with the CHF for horizontal channel flow boiling by Groeneveld et al. [31].

$$q''_{CHF,hor} = K_{hor} \times q''_{CHF,ver} \quad (22)$$

The horizontal inlet subcooling parameter, K_{hor} , depends on the value of the mass flux, G , shown in Eqn. (23).

$$K_{hor} = \begin{cases} 0 & G \leq G_{min} \\ \frac{G-G_{min}}{G-G_{max}} & G_{min} < G < G_{max} \\ 1 & G \geq G_{max} \end{cases} \quad \left. \vphantom{K_{hor}} \right\} \begin{array}{l} \text{Can be calculated from} \\ \text{Taitel et. al. equations} \end{array} \quad (23)$$

G_{min} : mass flux boundary between fully stratified and intermittent flow

G_{max} : mass flux boundary between intermittent and annular flow

4.3 MFBHF Analysis

Correlations by Simon [81] were used, as shown below, to analyze the MFBHF analytically. The correlations assume that the total heat flux is the summation of the convection heat flux (q_C) and the pool boiling heat flux (q_{PB}) shown in Eqn. (24).

$$q_{w,1} = q_C + q_{PB} \quad (24)$$

Furthermore, Simon states that in order to obtain the convection heat flux, Eqn. (25) is to be used, which is obtained from the Dittus-Boelter equation.

$$Nu = 0.024 Re_l^{0.8} Pr_l^{0.4} \quad (25)$$

The equation for pool boiling of liquid nitrogen is shown below in Eqn. (26).

$$q_{PB} = 4.87 \times 10^{-7} \left(\frac{c_{p,l}}{\Gamma \rho_v} \right)^{1.5} \left(\frac{k_l \rho_l^{1.282} P^{1.75}}{\sigma^{0.906} \mu_l^{0.626}} \right) \theta_1^{2.50} \quad (26)$$

Eqn. (27) and Eqn. (28) are used to find the MFBHF, where A could be 0.872 or 0.916, and where theta ($\theta_{q,w}$) is a function of pressure, fluid velocity, and heat flux obtained from Figure 4-1.

$$\theta_1 = (\theta_{2,\bar{h}})^* \quad (27)$$

$$(\theta_{2,\bar{h}})^* = \frac{1.84}{\theta_{q,w}} \left[T_c \left(0.13 \frac{P}{P_c} + A \right) - T_{sat} \right]^2 \quad (28)$$

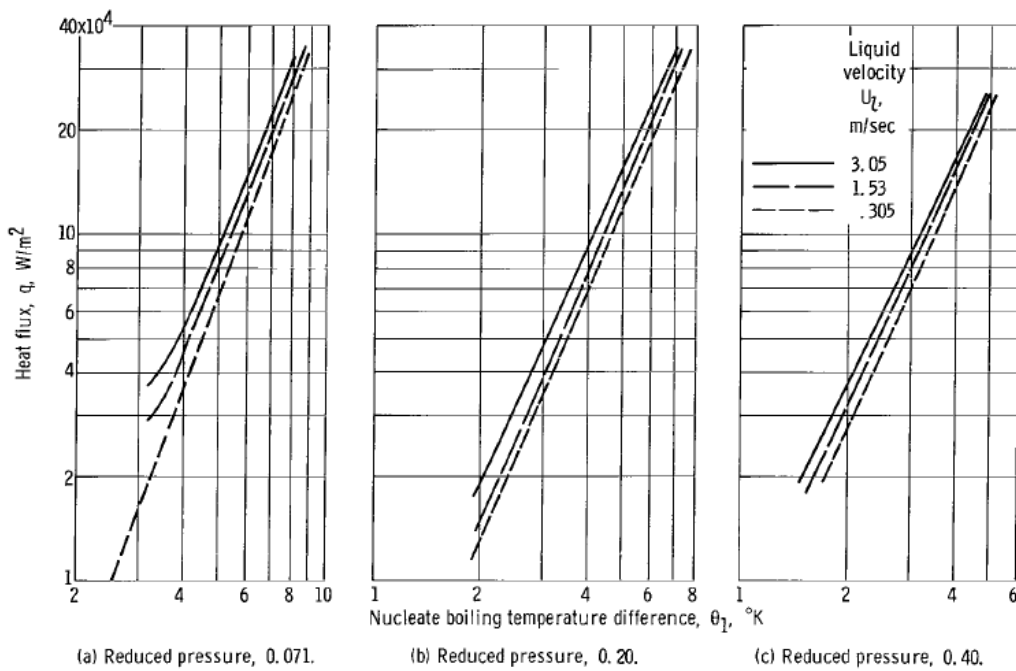


Figure 4-1. Nucleate boiling heat flux as a function of nucleate boiling temperature difference.

The typical minimum heat flux values obtained by Eqn. (23) are graphed in Figure 4-2, which is Eqn. (19) in [81]; the graph also includes Eqn. 10 from the literature.

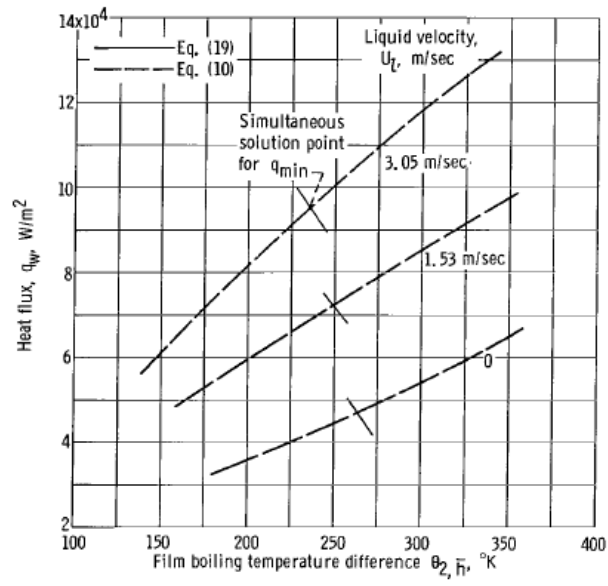


Figure 4-2. Typical graphical solution of the minimum heat flux. $\frac{P}{P_c} = 0.071, A = 0.872$

Chapter 5: Experimental Apparatus

5.1 High Heat Flux Test Facility

The experiments are performed under the influence of internal forced flow to better simulate the forced convective boiling performance in a rocket engine's combustion chamber environment. The Aerospace Center designed and developed the High Heat Flux Testing Facility (HHFTF) to conduct high-pressure cryogenic experiments, as shown in Figure 5-1. The HHFTF is a thermal concentrator system based on conduction that transfers heat onto a fluid by supplying a continuous asymmetrical heat flux to the test section resembling a regenerative cooling channel during combustion. Fluid conditions are monitored through the test duration using pressure and temperature instrumentation placed around the cooling channel test section. This concept is an adaptation of the Air Force's High Heat Flux Facility, described more in-depth by Bates, Irvine, and Maas [8, 33, 66].

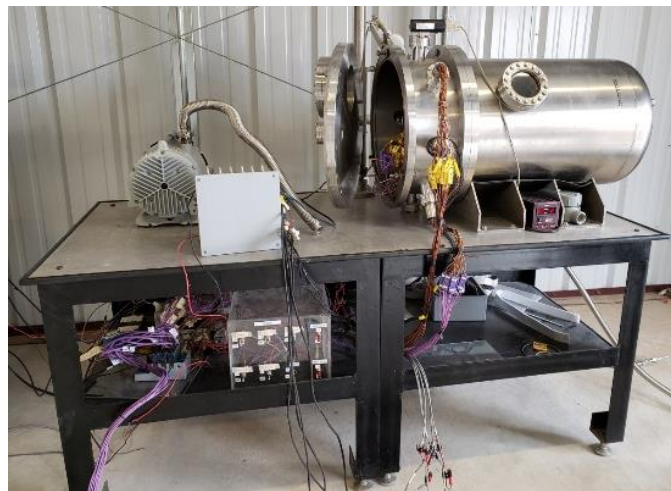


Figure 5-1. High Heat Flux Testing Facility.

The HHFTF is comprised of components including an assembled 316L stainless steel test stand, a cradle made of 6061-Al, a heating block made of C12200 copper with 17 slots on its sides

at the bottom to accommodate cartridge heaters, a 0.25” copper wafer located in between the heating block and cooling channel, and 3 test samples, shown in Figure 5-2.

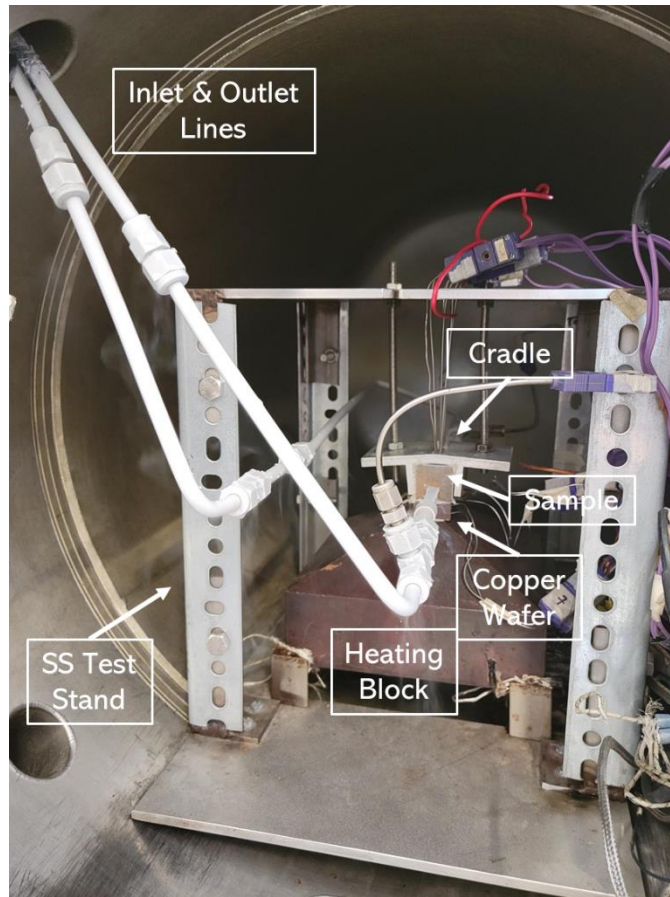


Figure 5-2. HHFTF inner assembly composed of inlet and outlet lines, stainless steel test stand, cradle, sample, copper wafer, and a heating block (lines are frosted from cryo temperatures).

Six grooves were machined on the wafer, as seen in Figure 5-3, to place thermocouples to obtain the temperature difference between the heating block and the sample to obtain the delta T needed for Fourier’s Law of Conduction.

Instrumentation incorporated in the HHFTF includes the following, a scroll vacuum pump (BOC Edwards XDS5), a Pirani gauge controller for the vacuum pump, 450W Watt-Flex cartridge heaters (Dalton Electric), a turbine flowmeter (Hoffer HO1/2X1/4A Series), a convection-enhanced Pirani sensor, static pressure transducers (Spectre Model 1000), and various

thermocouples. Temperature monitoring of the copper heating block was achieved with 17 type-K thermocouples (Dalton Electric 1 mm (0.04”)), which are placed on grooves already manufactured on the heating cartridges. Furthermore, six exposed tip type-E thermocouples (Omega 6.35 mm (0.25”)) were placed at the top of the sample to measure the wall temperatures through the length of the test section. A total of six exposed tip type-E thermocouples (Omega 1.5 mm (0.062”)) were placed on the grooves machined on the copper wafer to measure the temperature gradient across the wafer and obtain a temperature gradient needed for calculations. In addition, two ungrounded sheathed (304 SS, 3.0 mm sheath) type-E thermocouples were utilized to measure the bulk temperatures of the fluid. The locations of the thermocouples are shown in the schematic of Figure 5-3. Further component details can be found in Appendix A.

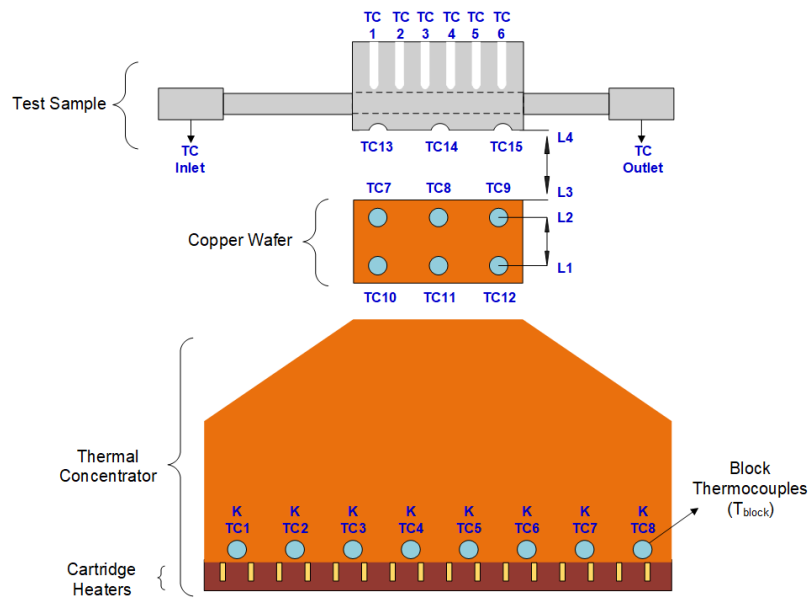


Figure 5-3. HHFTF inner assembly drawing composed of sample, copper wafer, and a heating block with thermocouples labels and placement (from top to bottom).

Finally, three static pressure transducers (PT) (Spectre) were placed at the inlet of the system, at the inlet of the channel, as well as the outlet to measure pressure drop, shown in Figure

5-4. A thermal standoff was placed in between the PT and the line with the fluid in order to prevent the cryogenic temperature from reaching the sensor since the temperature's lowest range is 233 K.

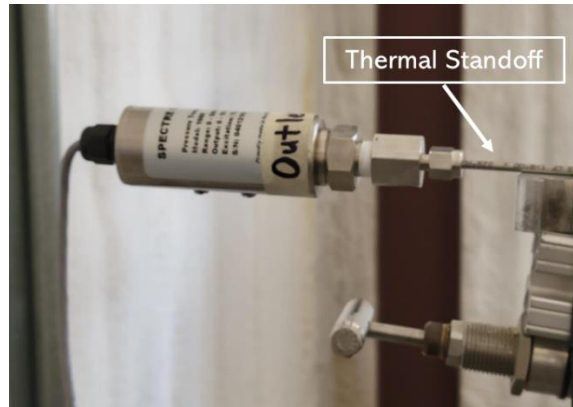


Figure 5-4. Pressure transducers for A) inlet of the system, and B) outlet of the channel.

In order to keep a constant pressure throughout testing, a constant pressure delivery system was used by using GN₂ to pressurize the dewar and maintain a constant pressure, shown in Figure 5-5.

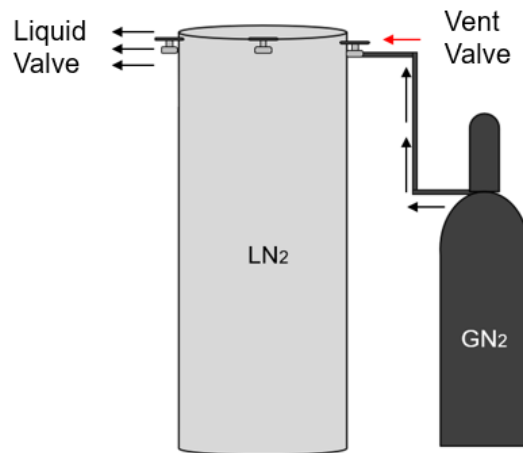


Figure 5-5. Constant pressure delivery system.

These experiments used a steady-state heating system through a variable transformer, VARIAC, where the current remained constant at 3 A and the voltage was adjustable to reach the

power desired, ranging from 0 to 130 V, shown below in Figure 5.6. It is important to note that during testing the highest voltage was 80 V.



Figure 5-6. VARIAC, variable transformer

5.2 Methane Condensing Unit

The HHFTF is incorporated with a methane condensing subsystem known as the Methane Condensing Unit (MCU) to achieve steady-state liquid methane (LCH_4) data. Figure 5-7 shows the MCU, which consists of a 13-liter condensing system used to liquefy gaseous methane (GCH_4) and provide the experiment with LCH_4 . In order to liquefy GCH_4 , a fluid that is colder than the LCH_4 saturation temperature needs to be utilized, such as liquid nitrogen (LN_2). In addition, gaseous helium (GHe) is also used, as seen in Figure 5-8, to keep the tank pressurized as it flows into the HHFTF system during testing.



Figure 5-7. MCU with liquid nitrogen dewar.

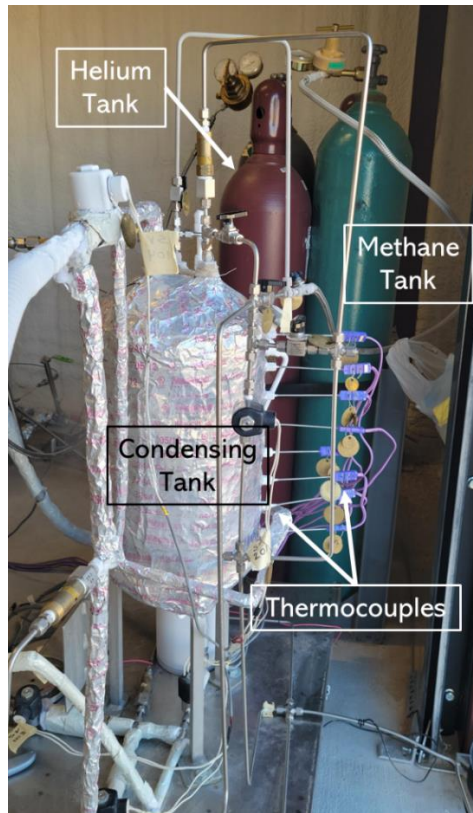


Figure 5-8. Methane and helium tanks.

Components for this test facility consist of one cryogenic pressure transducer, pressure relief valves, solenoid valves, manual valves, and thermocouples. The tank is configured as a shell and coil heat exchanger with a 316 Stainless Steel outer shell. The tank has a maximum allowable working pressure of 3.4 MPa, which allows the tank to sustain cryogenic temperatures. An 18.3 m coil with a 3.35 mm outer diameter made of stainless steel tubing is inside the tank. As the LN₂ flows through the inner coil, LCH₄ is condensed within the tank. In addition, the tank is wrapped with 30.5 m with a 6.35 mm outer diameter copper tubing. LN₂ also flows through the outer copper tubing to cool the tank walls. In addition, the copper tubing is covered with several layers of cryogenic insulation. Eight thermocouples (Omega) are placed inside ports located vertically along the tank to measure the LCH₄ temperatures in the tank; this can be seen in Figure 5-9. Lastly, a thin-film cryogenic PT (Omega PX1005L1) is located at the top of the tank to supervise the pressure.

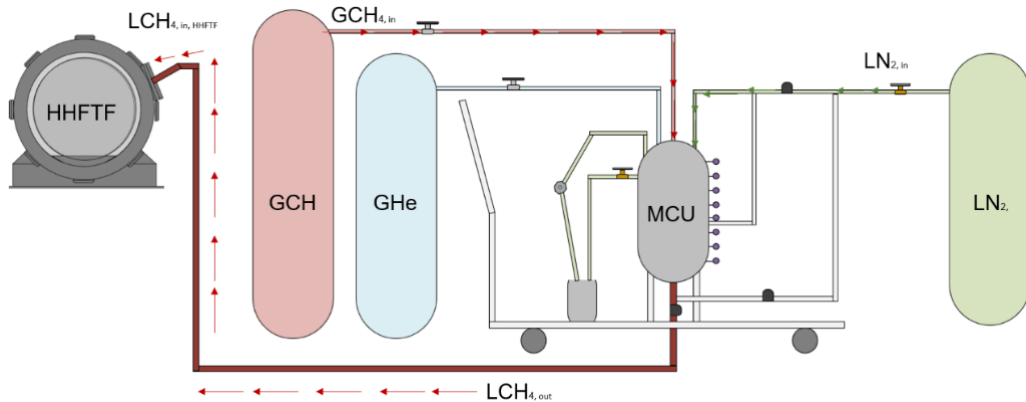


Figure 5-9. Methane condensing unit with fluids and schematic to HHFTF.

5.3 Experimental Method: Test Procedures

The procedure for this test was designed to keep the safety guidelines for the facility and the test conductors. All personal protective equipment was used when handling cryogenics, tripping hazards were minimized, and leaks were found and fixed to protect the test conductors.

The test procedure begins with placing the desired test sample onto the test rig and running a leak check of the entire system and an instrumentation check to ensure all measurements are connected and read correctly. Next, the test sample is inside a vacuum chamber that is evacuated and held at a vacuum of about 19×10^{-2} Torr (3.6×10^{-3} psi) to remove all air that could conduct heat away from the sample. Then, the sample and delivery lines are chilled with LN₂ for approximately two hours to reach the appropriate inlet conditions.

The heating process begins with the VARIAC at the minimum voltage allowable and increases the power applied to the system in steps ranging between 300 and 500 Watts. The voltage is increased while the current remains constant at 3 A, in intervals until the critical heat flux (CHF) is reached, which is identified by a spike in temperature in thermocouples TC13 – TC15 located under the sample.

Subsequently, the power is decreased in steps beginning with approximately 800 to 1000 Watts and proceeding to a lessening in power of 200 to 400 Watts until the MFBHF is reached. That means we reached the point where the fluid goes from the film boiling regime back to the nucleate boiling regime.

5.4 Data Analysis

The data was collected using the LabVIEW software; the virtual instrument's (VI) front panel for the delivery system is shown in Figure 5-10. The VI block diagram uses an Express VI for a more accessible user interface. The VI monitors the instrumentation, consisting of three PTs, many thermocouples, and a flow meter installed on the main line.

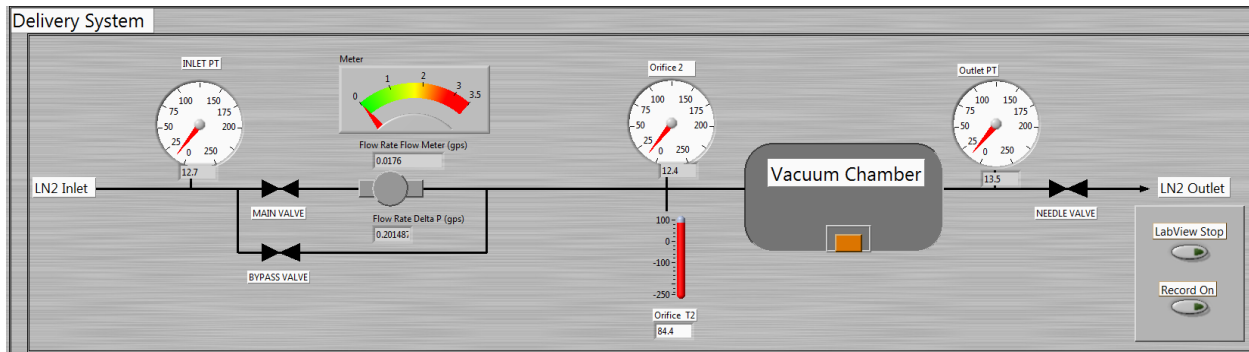


Figure 5-10. Instrumentation of the delivery system for the HHFTF consisting of thermocouples, pressure transducers, and a flow meter.

Figure 5-11 shows the thermocouples placed on the test sample and the ones placed on the heating block. Also shown is the heat flux of the wafer and the channel. Lastly, it shows the average temperature of the top and bottom thermocouples on the copper wafer, separately, $Average(TC\ 7,8,9)$ and $Average(TC\ 10,11,12)$.

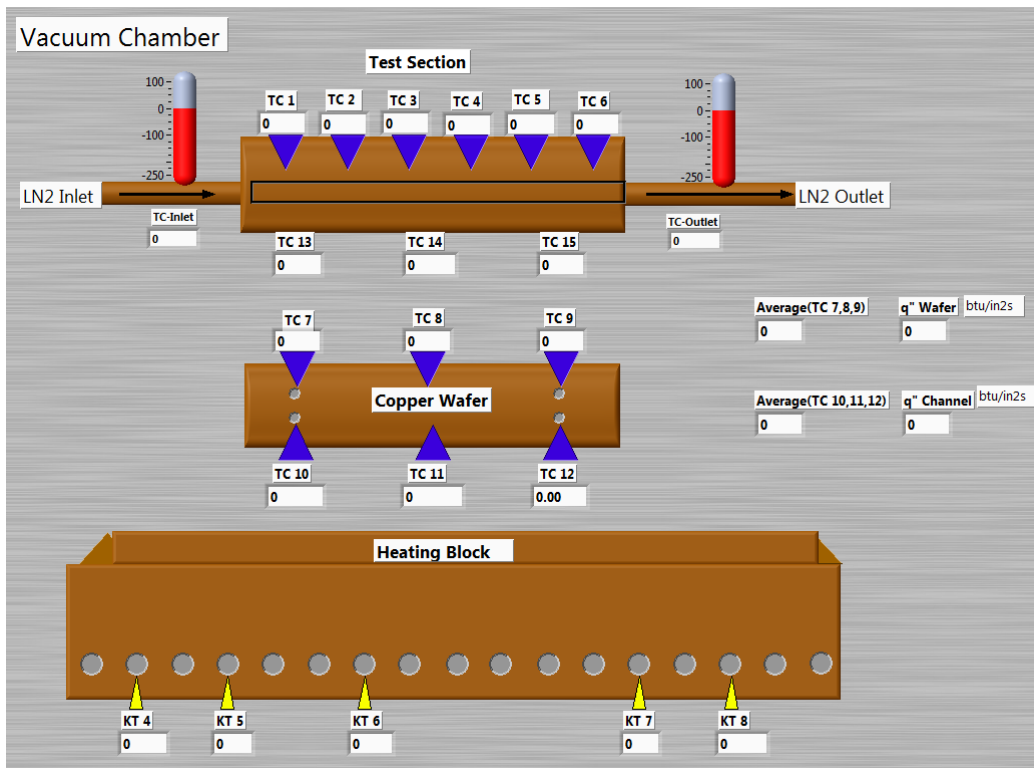


Figure 5-11. Thermocouples inside the vacuum chamber.

The last image of the front panel can be observed in Figure 5-12, showing the thermocouples used to monitor the MCU. These thermocouples allow the temperature reading of the fluid inside the tank to determine its phase; the goal is fully liquid.

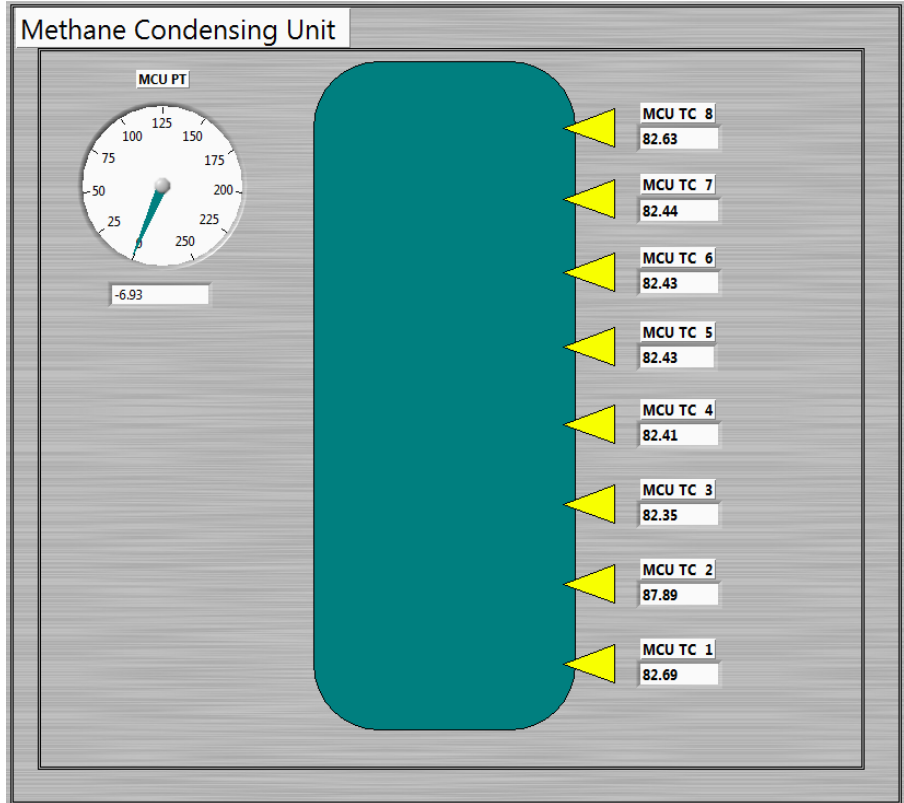


Figure 5-12. Thermocouples for the MCU.

5.5 Uncertainty Analysis

The results collected depended on the instrumentation accuracy per the manufacturer, hence the need for an uncertainty analysis; refer to Table 5.1 for the percent error [32]. Eqn. (29) displays the uncertainty propagation and was used to calculate the overall error. Instrumentation was affected by various factors; the pressure transducers and the flow meter were affected by the calibration and phase of the fluid. Additionally, REFPROP has a $\pm 0.2\%$ accuracy; this Excel add-

in was used for obtaining the fluid’s properties, such as density and latent heat under specific temperature and pressure conditions. All instrumentation can be found in Appendix A.

$$(U_{cal}) = \sqrt{\sum \left(\frac{\delta f(\text{Calculated})}{\delta \text{Variable}} \text{Error}_{\text{variable}} \right)^2} \quad (29)$$

TABLE 5-1. INSTRUMENTATION MEASUREMENT ACCURACY

Measured Parameter	Percent Error
Turbine Flow Meter	±0.10
Pressure Transducers	±0.25
Thermocouples	±1.00
REFPROP	±0.20
Pressure Differential	±0.35
Temperature Differential	±1.40
Mass Flow Rate	±1.23
Heat Transfer Coefficient	±2.42
Heat Flux	±2.64
Measured Nusselt Number	±6.20

Chapter 6: Experimental Results

6.1 Single-Phase Forced Convection

Four samples, shown in Figure 6-1, were made from Inconel 625 with a D_h of 3.2 mm and were tested to characterize the single-phase forced convective heat transfer [72]. Three samples were manufactured conventionally with various surface roughness of 0.8, 3.2, and 6.3 microns. The fourth sample was additively manufactured with a surface roughness of 12.5 microns.

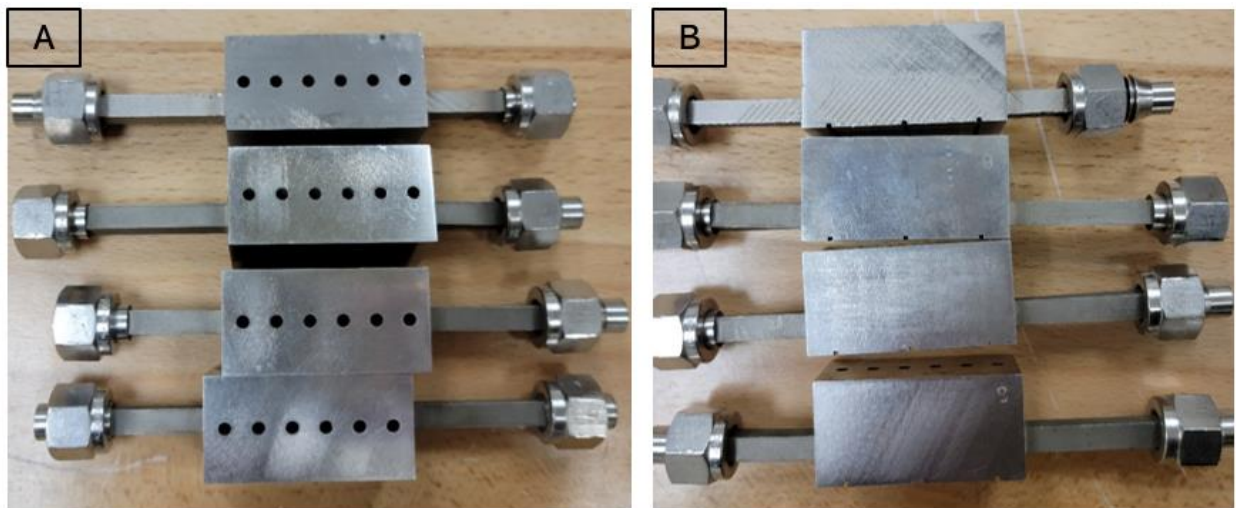


Figure 6-1. Samples made from Inconel 625. A) Top view, B) Side view with grooves on the bottom.

The testing procedure for these samples required the system to be cooled down for one to two hours to ensure the fluid remained fully saturated. Next, heat was applied to the sample with a constant heat flux. The single-phase forced convective heat transfer can be seen below in Figure 6-2 with a graph of the heat flux as a function of the difference between the wall temperature, T_{wall} , and the fluid temperature, T_{fluid} . The heat flux is separated by sample; red pertains to INCO 12.5, blue to INCO 6.3, green to INCO 3.2, and black to INCO 0.8. The maximum heat flux obtained was for the sample with the highest surface roughness with a heat flux of 791 kW/m^2 and a temperature difference of about 72 K. This value has more than a 200% enhancement in heat flux

for that specific delta T compared to literature. Additionally, while the sample with the highest surface roughness has the highest values, the channels with the lower roughness values have a lower limit.

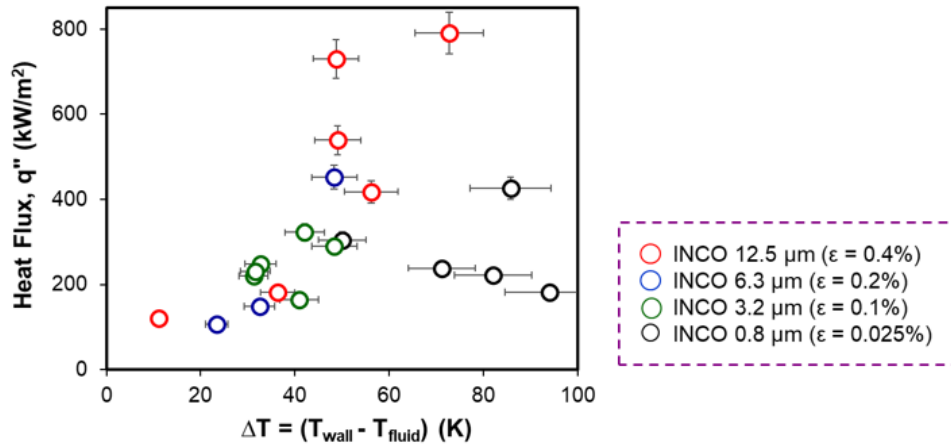


Figure 6-2. Forced convection results. Heat flux as a function of delta T = (T_{wall} – T_{fluid}).

Further data analysis was done to find the respective HTC values; Figure 6-3 shows the data for the HTC as a function of delta T. The maximum value was found at 10 kW/m²K with a delta T of about 72 K, obtained by the channel with the highest surface roughness of 12.5 microns. The HTC values are similar to the heat flux values from Figure 6-2. There is more than a 150% enhancement with HTC at that given delta T.

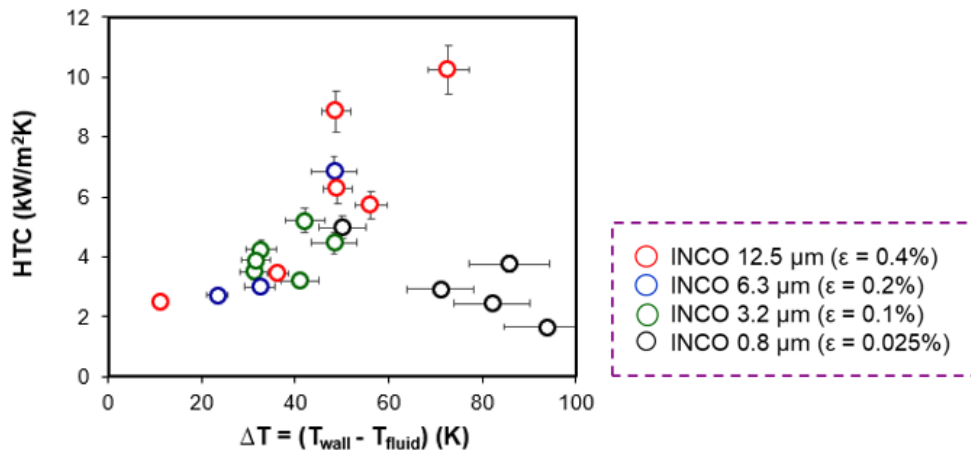


Figure 6-3. HTC as a function of delta T = (T_{wall} - T_{fluid}).

Another factor to consider is the pressure drop across the channel. Figure 6-4 shows the pressure drop as a function of the Reynolds number Re , shown in Eqn. (30), where ρ is the fluid density, V is the fluid velocity, D is the pipe diameter, and μ is the dynamic viscosity. The Re varies from around 45,000 to almost 120,000 for all samples, while the pressure drop remains at about 10 to 40. The conclusion can be made that regardless of the flow rate, because the pressure drop remained constant, it is not a critical property to worry about.

$$Re = \frac{\rho V D}{\mu} = \frac{G D}{\mu_l} \quad (30)$$

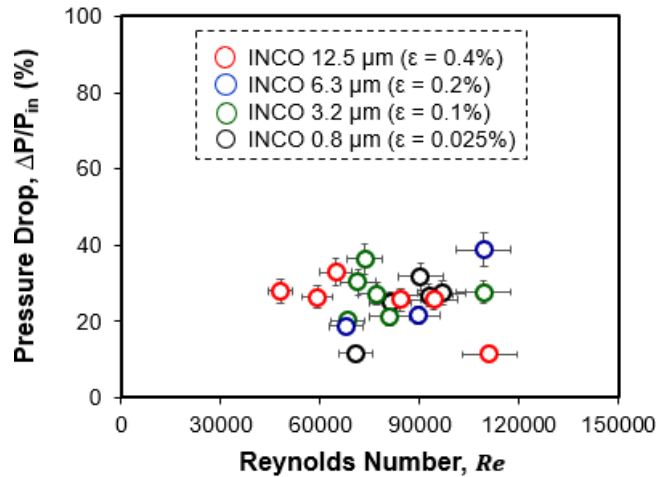


Figure 6-4. Pressure drop as a function of Reynolds number.

Lastly, the experimental Nusselt number for the four samples was compared to the NASA Rocketdyne correlation, Dittus-Boelter model, Sieder-Tate model, and Gnielinski correlation. These correlations. Figure 6-5 shows a plot with these correlations compared to the experimental results for the four samples; all the thermophysical properties were obtained using the NIST REFPROP 8.0 software.

A pattern can be seen that as the Nusselt number increases, so does the Reynolds number. In Figure 6-5, it can be seen that there is an enhancement of 200% in the Nusselt number in the highest flow rate from INCO 6.3 μm ($\epsilon=0.2\%$) to INCO 12.5 μm ($\epsilon=0.4\%$). The NASA Rocketdyne correlation aligns with INCO 12.5 as the Reynolds numbers and Nusselt numbers increase but it is less accurate with lower values. The correlation that aligned the best with the average of all the data points is the Dittus-Boelter model and the Sieder-Tate model. For INCO 0.8, the Gnielinski correlation aligned the best, although those values are not desired. Nonetheless, this proves that these models cannot be used individually throughout all the different conditions; they rely on the different surface roughness and flow rates. Further explanation of each correlation can be found in Section 4.1.

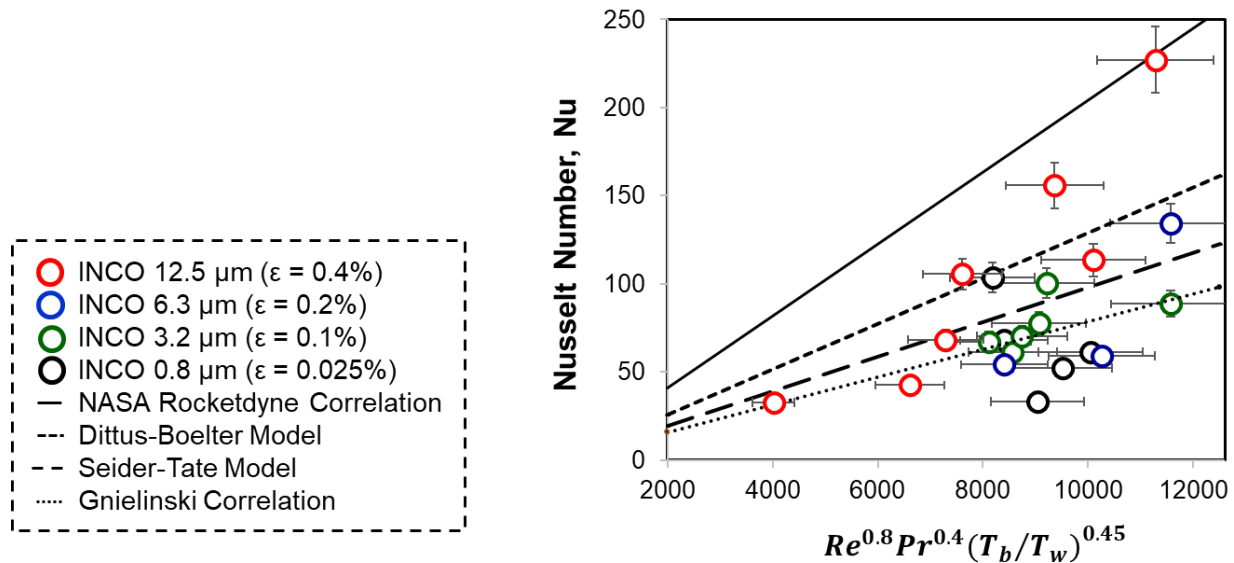


Figure 6-5. Experimental Nusselt numbers plotted with NASA Rocketdyne correlation, Dittus-Boelter model, Sieder-Tate model, and Gnielinski correlation

6.2 Forced Convective Boiling

Forced convective boiling happens when a pressurized fluid flows through a channel and heat is applied, as described in Sections 1.3 and 3.1. This section will concentrate on how the CHF

and MFBHF were detected in the data, the results of the tests for all three GRCop-42 samples, and the effect of mass flux, hydraulic diameter, pressure, degree of subcooling, type of fluid, and surface roughness. Lastly, it will go over some comparisons with models. Shown below on Table 6-1, is the flow boiling test matrix for conducting the experiments.

TABLE 6-1. FLOW BOILING TEST MATRIX

Hydraulic Diameter	Pressure (MPa)	Subcooled Degree (K)	Mass Flux (cm ³ /s)
D _h ~ 1.8 mm	1.37	0	31.5, 47.5, 56
	1.58	0, 5	31.5
D _h ~ 2.3 mm	1.37	0, 5	31.5, 47.5, 56, 82
	1.58	5	31.5
D _h ~ 2.5 mm	0.89	0	82
	1.37	0	31.5, 47.5, 56
	1.58	0	31.5

6.2.1 CHF/DNB Detection

The CHF point, or departure from nucleate boiling, is defined as the stage when the interface is covered with a thin vapor film, causing a spike in the surface temperature. For experimental purposes, the spike in temperature determines when the CHF point has been reached; the flow rapidly transitions from annular to mist flow and then thoroughly vaporizes. As shown in Figure 1-4 in Section 1.3.5, the theoretical transition from point B to point C keeps a constant heat flux while the temperature increases. Experimentally, the graph is expected to look similar to Figure 6-6, as discovered by VanNoord [87]; the heat flux is expected to keep increasing with a change in slope to be expected.

Figure 6-7 shows two graphs with the heat flux as a function of the temperature difference (left) and the temperature of thermocouples T13, T14, and T15 (right). The change in slope can be

seen where the CHF is detected at 387 kW/m^2 , signifying a rapid rise in temperature of the fluid as it changes phases from liquid to vapor; hence the fluid transitions from nucleate boiling to film boiling. On the right graph, the highest temperature increase can be seen on T13, with an increment of 86 K above the saturation temperature.

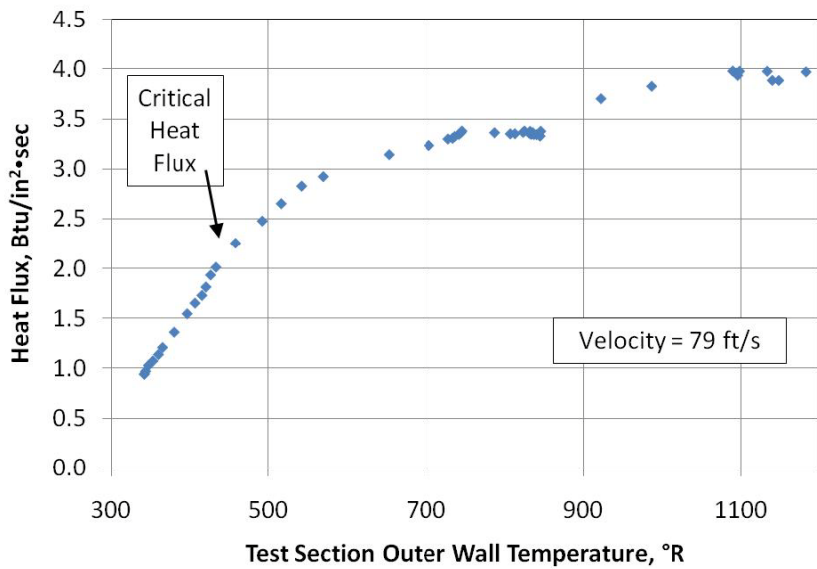


Figure 6-6. Typical test section response for increasing heat flux found by VanNoord [87].

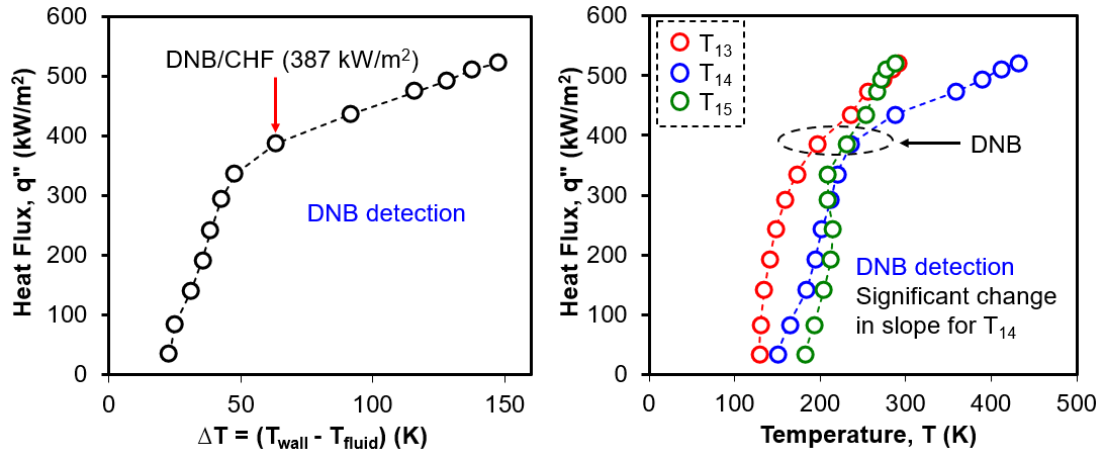


Figure 6-7. Heat flux as a function of temperature different (delta T) and temperature in K.

Calculations were done to verify the values selected to solve for the highest difference between each data point recorded and calculate the slope change to verify the dips and spikes. For this case, the greatest slope change happened on T14 (blue) from 3.2 to 0.94; on average, for all three thermocouples, the slope change was from 2.6 to 1.4.

6.2.2 MFBHF Detection

The MFBHF occurs when the fluid changes from a film boiling regime back to nucleate boiling, and bubbles reappear, replacing the vapor film covering the surface. In the previous section, a significant temperature increase determined if the CHF had been actualized; similarly, for the MFBHF, a remarkable drop in temperature is what determines that the minimum heat flux has been reached. As we decreased the power level on the VARIAC, sufficient time (about 5 to 10 min) was permitted to note whether nucleate boiling would appear at any of the thermocouples.

Figure 6-8 has two graphs; the graph on the left is the heat flux as a function of delta T, where the change in slope can clearly be seen at 352 kW/m² as the fluid changes from film boiling back to nucleate boiling.

The graph on the right of Figure 6-8 shows the heat flux as a function of temperature, where the greatest change can be seen on T15 with a temperature drop of 174 K to 127 K above saturation. The calculation for slope change was used to verify the MFBHF; the slope changed from 0.96 to 4.7 on T15, and the average slope change for all three thermocouples was from 1.4 to 3.3, which is the expected change. The MFBHF was taken at the lowest power level, which allowed film boiling to remain over the surface.

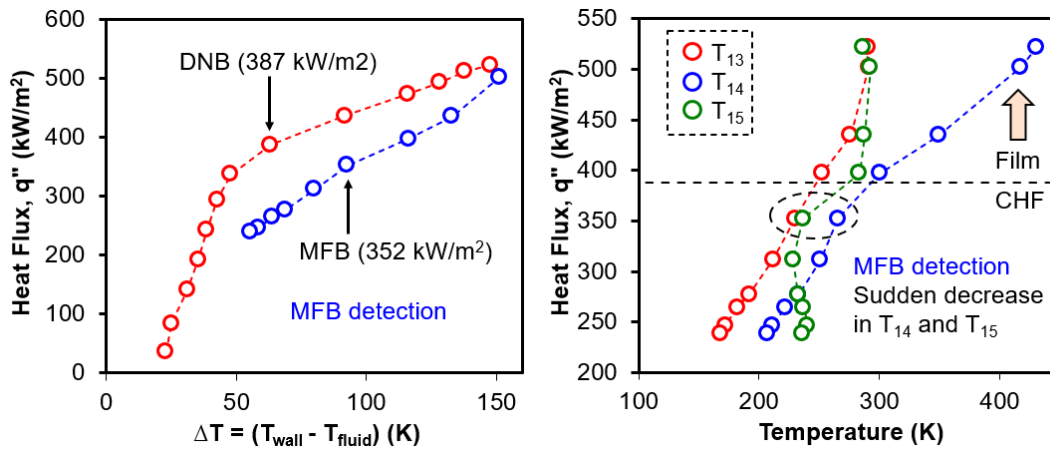


Figure 6-8. Heat flux as a function of delta T and temperature in K.

Lastly, boiling hysteresis is the phenomenon where the value of heat flux lags behind as its coming back down, and can sometimes be confused as MFBHF. Figure 6-9 shows an experiment that proved that the HHFTF has no boiling hysteresis since it has no lag, and the data points obtained are accurate.

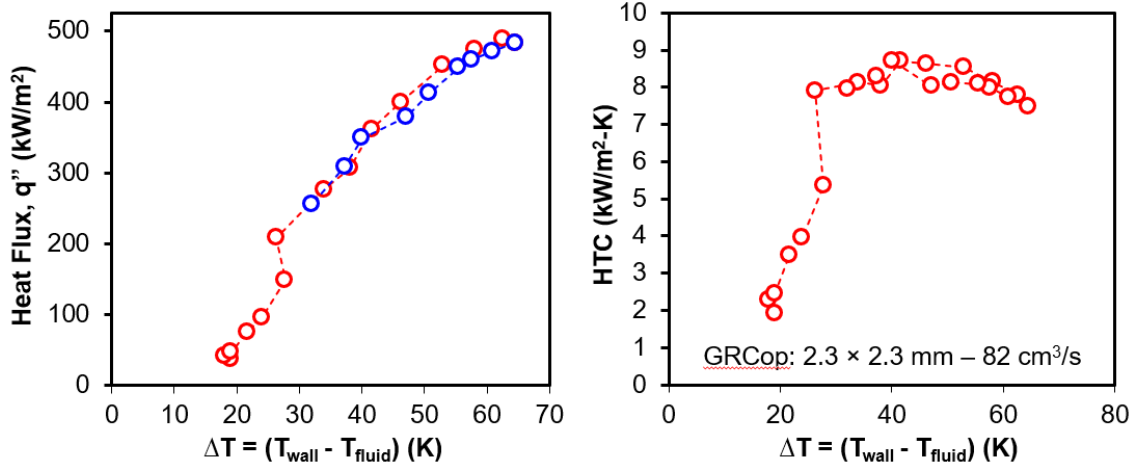


Figure 6-9. Boiling Hysteresis tested up to 489 kW/m² with no CHF.

6.2.3 Results for D_h = 2.5 mm Channel

Tests were completed to characterize the cooling properties and heat transfer efficiency of several different channel dimensions with additively manufactured samples from GRCop-42. The results for the sample with a channel dimension of 1.8 mm X 2.3 mm and a hydraulic diameter of 2.5 mm are shown in Figure 6-10. The values for the flow rates, CHF, and MFBHF are shown in Table 6-1. The CHF and MFBHF increase as the flow rate increases, but these values have the lowest performance compared to the following two samples. Additionally, the HTC follows the same pattern where the CHF point is the limit of the sample’s efficiency, and from then on, it decreases, which is expected since the liquid is replaced with vapor.

TABLE 6-1. CHF AND MFBHF RESULTS FOR SAMPLE DH = 2.5 MM

Volumetric Flow Rate (cm ³ /s)	CHF (kW/m ²)	MFBHF (kW/m ²)
31.5	221	167
47.5	285	220
57	307	253

6.2.4 Results for $D_h = 2.3$ mm Channel

The results for the second sample with a channel dimension of 2.3 mm X 2.3 mm, and a D_h of 2.3 mm are shown in Figure 6-11. The values for the flow rates, CHF, and MFBHF are shown in Table 6-2. In an attempt to test at 31.5 cm³/s, the allowable flow for those two tests was 38 cm³/s, which is why it was added to the matrix. The values follow the same pattern, that as the flow rate increases so does the limit for the heat flux.

TABLE 6-2. CHF AND MFBHF RESULTS FOR SAMPLE $DH = 2.3$ MM

Volumetric Flow Rate (cm³/s)	CHF (kW/m²)	MFBHF (kW/m²)
31.5	337	288
38	387	352
38	401	339
47.5	445	391
47.5	426	359
57	459	379

6.2.5 Results for $D_h = 1.8$ mm Channel

Figure 6-12 shows the results for the third sample of 1.8 mm X 1.8 mm with a D_h of 1.8 mm. The values for the flow rates, CHF, and MFBHF can be seen in Table 6-3. Something important to note is that as the flow increases, so do the CHF and the MFBHF; also the heat transfer stays approximately the same for 31.5 cm³/s and 47.5 cm³/s, but it increases by 175% for 57 cm³/s. This proves that the higher flow rate performs best for the smallest sample. Following the analysis, it is concluded that this is the most efficient sample.

TABLE 6-3. CHF AND MFBHF RESULTS FOR SAMPLE $DH = 1.8$ MM

Volumetric Flow Rate (cm ³ /s)	CHF (kW/m ²)	MFBHF (kW/m ²)
31.5	465	390
47.5	543	486
57	768	719

6.2.6 Effect of Mass Flux

The effect of mass flux on the CHF and MFBHF for all three samples is shown below in Figure 6-10 and Figure 6-11. The operating pressures for these tests were 1.37 MPa (200 psi) and 1.58 MPa (230 psi). These graphs show the relation of mass flux with respect to the CHF, and MFBHF, and how it changes with the two different pressures. As the pressure increases, the CHF/MFBHF values drop, but as the flow rate, or mass flux, increases, it also increases the CHF/MFBHF. Plots separated by sample can be found in Appendix B. The highest heat flux values were seen on sample with a D_h of 1.8 mm, the red circles. The highest CHF value was 768 kW/m² with a mass flux of 14,295 kg/m²s; the highest MFBHF value was 719 kW/m² with a mass flux of 14,295 kg/m²s.

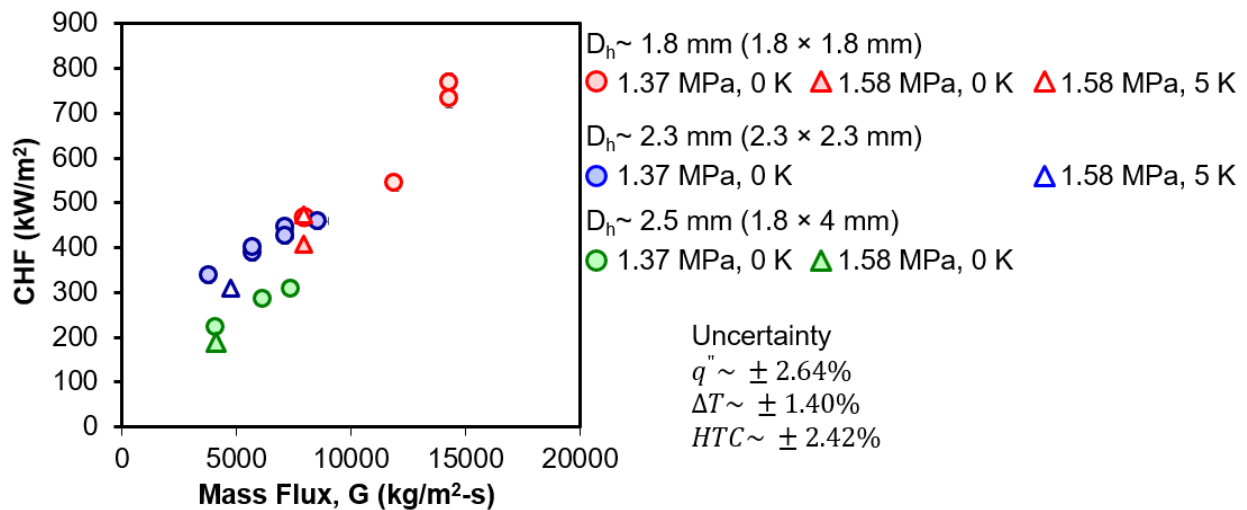


Figure 6-10. CHF as a function of mass flux for all three samples.

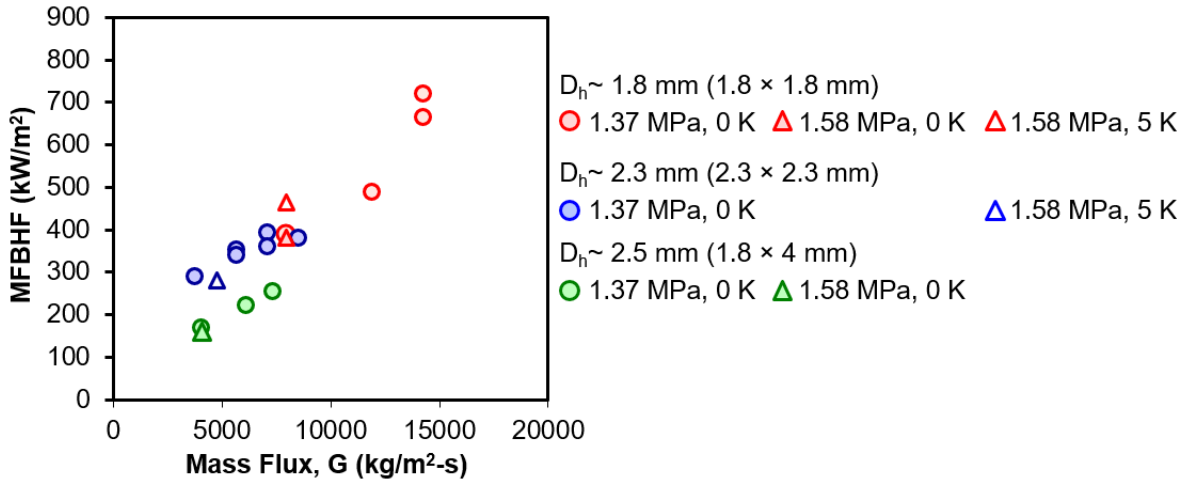


Figure 6-11. MFBHF as a function of mass flux for all three samples.

6.2.7 Effect of Hydraulic Diameter

Another factor considered was the hydraulic diameter. As seen in Figure 6-12, the values with the highest CHF and MFBHF are the ones pertaining to the D_h = 2.3 mm sample with 459 to 379 kW/m², respectively. Meanwhile, the sample with D_h = 2.5 mm stays with maximum values of 307 to 253 kW/m².

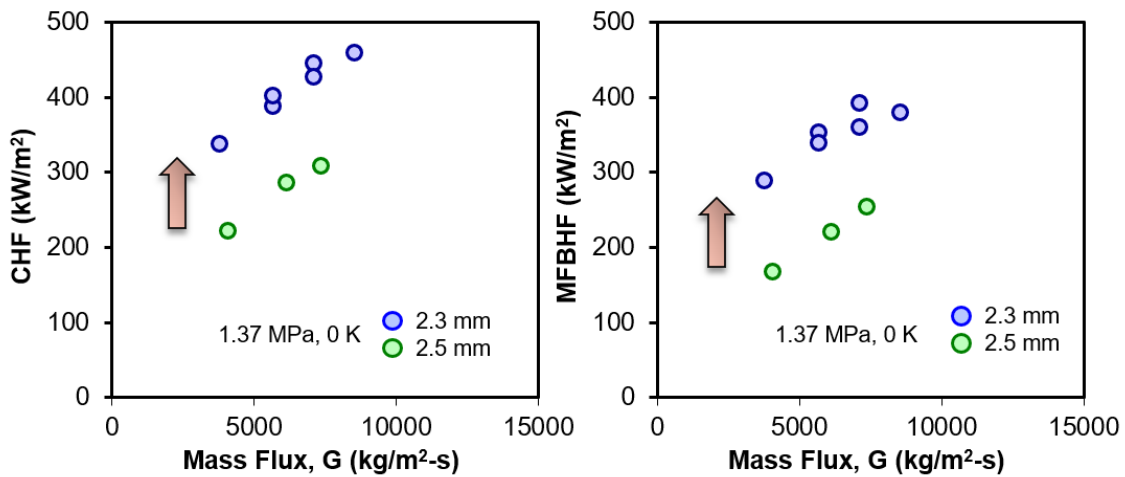


Figure 6-12. Effects of hydraulic diameter on CHF and MFBHF as function of mass flux.

Heat flux is a ratio of the mass flux times the latent heat divided by the Reynolds number, as shown in Eqn. (31). The Reynolds number equation is shown in Eqn. (30).

$$q''_{CHF} = \frac{C_c G h_{lv}}{Re^{0.5}} \quad (31)$$

Since the Reynolds number is directly proportional to the diameter, the CHF is inversely proportional to the diameter, which can be seen in Eqn. (32), meaning that as the diameter increases, the heat flux will decrease, so the smaller the channel, the better.

$$q''_{CHF} \propto \frac{1}{D^{0.5}} \quad (32)$$

Even though a small channel is desired, it is important to note there is a limit driven by the capillary length for LN₂, shown in Eqn. (33). A channel smaller than 0.6 mm enters into the microchannel category, which requires a different theoretical analysis.

$$\lambda_{LN2} = \sqrt{\frac{\sigma}{(\rho_l - \rho_v)g}} = 0.6 \text{ mm} \quad (33)$$

6.2.8 Effect of Pressure

The operating pressure for the tests was 1.37 MPa (200 psi) and 1.58 MPa (230 psi), with a pressure drop ranging from 10 to 25% throughout all the tests. Figure 6-13 shows the CHF and MFBHF as a function of mass flux with the two different pressures, which are circled. For the CHF graph on the left, the heat flux is lower for a higher pressure for both samples with Dh = 1.8 and 2.5 mm. This behavior is attributed to the relationship between heat flux and the latent heat of vaporization, as they are directly proportional, as seen in Eqn. (31) and Eqn. (34).

$$q''_{CHF} \propto h_{lv} \quad (34)$$

If the latent heat is greater, it can gather more energy before the fluid changes phases from liquid to vapor, allowing for a greater CHF. Inversely, as pressure climbs, the latent energy

declines along with the heat flux, as seen in Eqn. (35). The uncertainty for the heat flux was calculated to be $\pm 2.64\%$.

$$P \uparrow \sim h_{lv} \downarrow \quad (35)$$

This pattern can be seen on the graph on the right with the MFBHF, where the heat flux is slightly lower for the higher pressure.

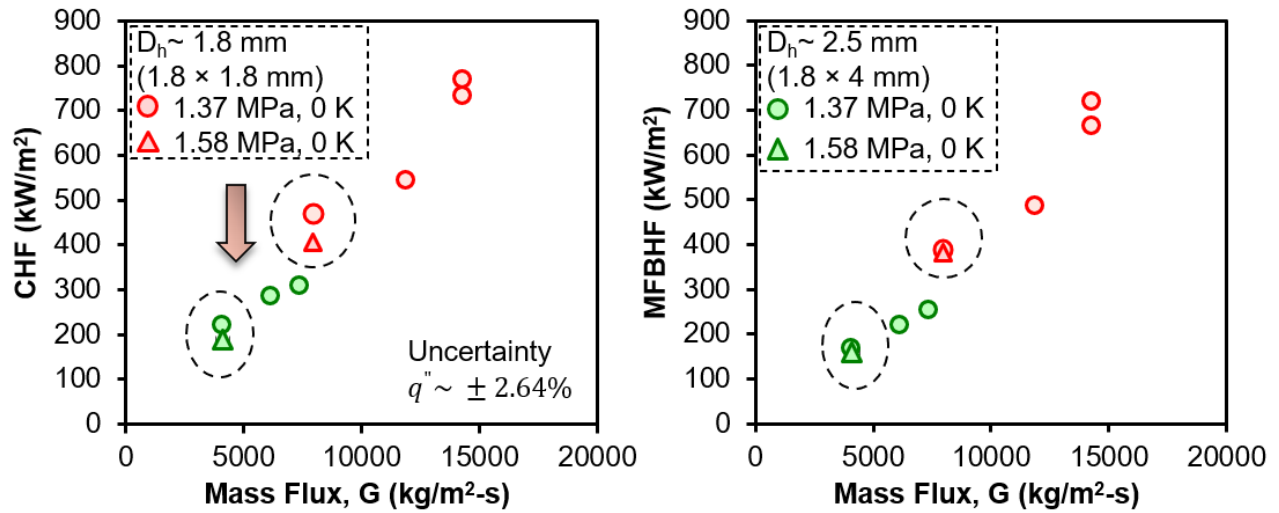


Figure 6-13. Effects of pressure on CHF and MFBHF as a function of mass flux.

6.2.9 Effect of Degree of Subcooling

Although reaching a subcooling lower than 0 was challenging, the higher degree of subcooling allows for better thermal management, capitalizing on the sensible and latent heat and delaying the CHF occurrence, as described by Lee et al. [59]. Figure 6-14 shows how for the sample of a hydraulic diameter of 1.8 mm, the data point with a subcooled degree of 5 K has a higher CHF value. The greater the degree of subcooling is, meaning a colder fluid, the higher the viscosity, as shown in Eqn. (36). Given that the property is higher for a liquid than a vapor, it allows for a lower Reynolds number, as seen in Eqn. (30).

$$T_{LN2} \downarrow \sim \mu_{LN2} \uparrow \sim Re \downarrow \quad (36)$$

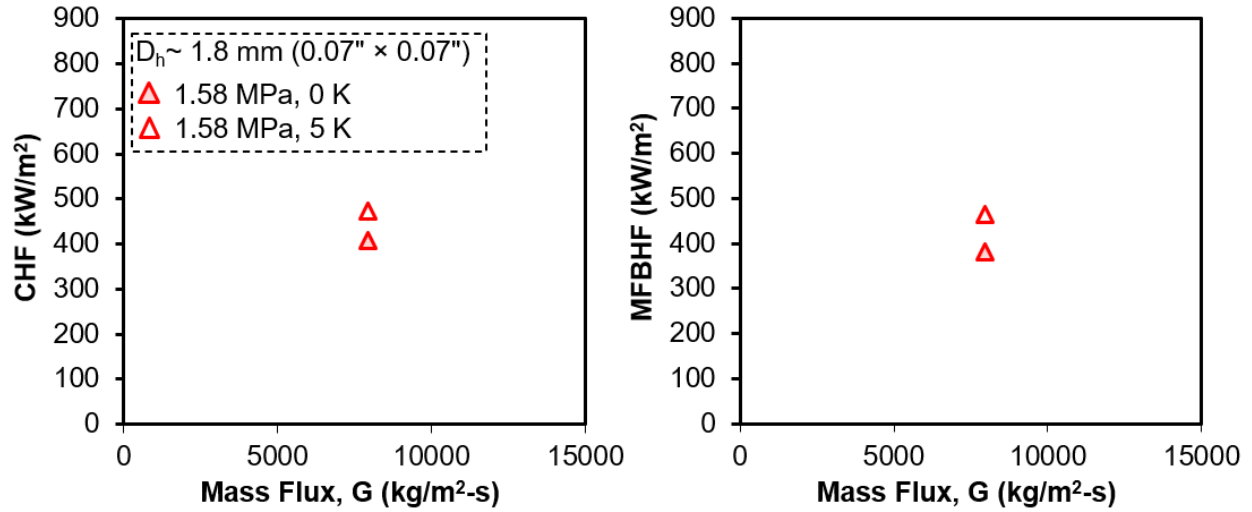


Figure 6-14. CHF and MFBHF as a function of mass flux with 0 and 5 K degree of subcooling.

Furthermore, since high pressures are required, as that is the environment in a regeneratively-cooled engine, a way to find a balance is to increase the subcooling degree while increasing pressure. Figure 6-15 depicts the effect of an increase in pressure and subcooling degree. The best performance was seen in the sample with a $D_h = 1.8$ mm, proving that the change in the subcooling degree allowed the CHF to remain constant at higher pressure, unlike in Figure 6-14. For the MFBHF the heat flux value actually increased, further proof this is a good way to increase the limits of the channels.

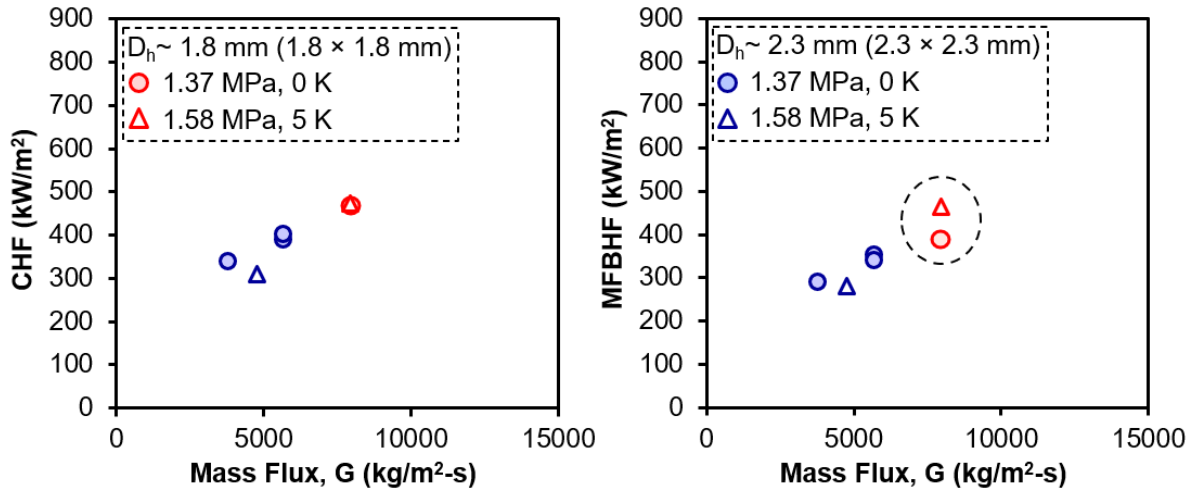


Figure 6-15. CHF and MFBHF as a function of mass flux with the effect of combined pressure and subcooling degree.

6.2.10 Effect of Fluid

Two different cryogenic fluids were used for this investigation, LN₂ and LCH₄. Figure 6-19 presents the comparable values for LN₂ and LCH₄ testing. The LCH₄ testing was only performed on the sample with a hydraulic diameter of 2.3 mm; further testing needs to be done to verify if the pattern occurs on the other two hydraulic diameters. Nonetheless, as shown in Figure 6-16, the CHF and MFBHF are significantly higher, with approximately a 150% enhancement even with a lower mass flux.

The enhancement is derived from latent heat of vaporization, as the value is greater for LCH₄, so it is able to collect more energy. Also, the viscosity is less for LCH₄ than LN₂, leading to a higher Reynolds number for LCH₄. Methane is of greater interest in the industry since it can potentially be extracted from the moon and planets in space, which will ideally allow deeper space exploration.

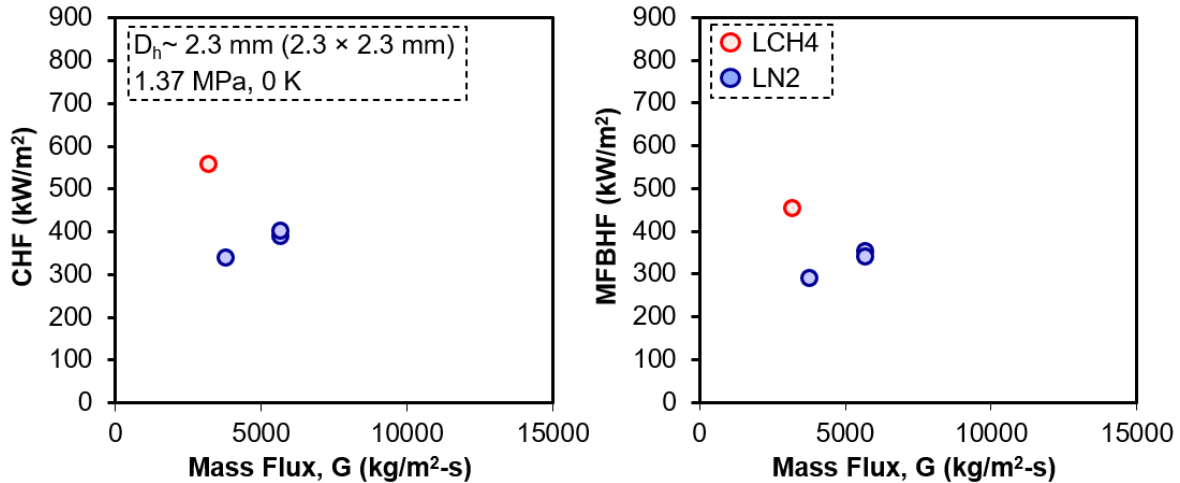


Figure 6-16. CHF and MFBHF as a function of mass flux with LCH₄ and LN₂ at 1.37 MPa.

6.2.11 Effect of Surface Roughness

The effect of surface roughness was characterized in Section 6.1 by showing the enhancement in heat flux with the additively manufactured sample of 12.5 microns with a sample made from Inconel 625. Unfortunately, time challenges prevented the analysis of the specific value of surface roughness for the GRCop-42 samples. Nonetheless, based on the results found by forced convection, it can be assumed that surface roughness, as it increases surface area, enhances boiling as well.

6.2.12 Comparison with Models

Theoretical values were calculated for all three samples to compare to the experimental results. The CHF model values for each sample with its respective mass fluxes are shown in Table 6-4. The expected CHF model values are shown in Figure 6-17 with the various flow rates, pressures, and subcooling degrees for all three samples; these values were obtained using Eqn. (6) through Eqn. (23). Experimental results show an enhancement from the model values; specifically,

the values from the sample with $D_h = 1.8$ mm delivered a 98% enhancement with a CHF value of 14,295 kW/m^2 .

TABLE 6-4. MODEL CHF VALUES FOR ALL THREE SAMPLES AT 1.37 MPa, 0 K

Hydraulic Diameter (mm)	Mass Flux ($\text{kg/m}^2\text{s}$)	CHF (kW/m^2)
1.8	7941.87	317.3979
	8561.54	320.6094
	11912.61	335.1192
	14295.61	343.40
2.3	3805.46	273.8867
	4756.52	282.1975
	5707.83	289.1768
	7134.79	297.9541
2.5	8561.74	305.3231
	4105.07	272.1193
	6158.65	287.3197
	7389.96	294.4235

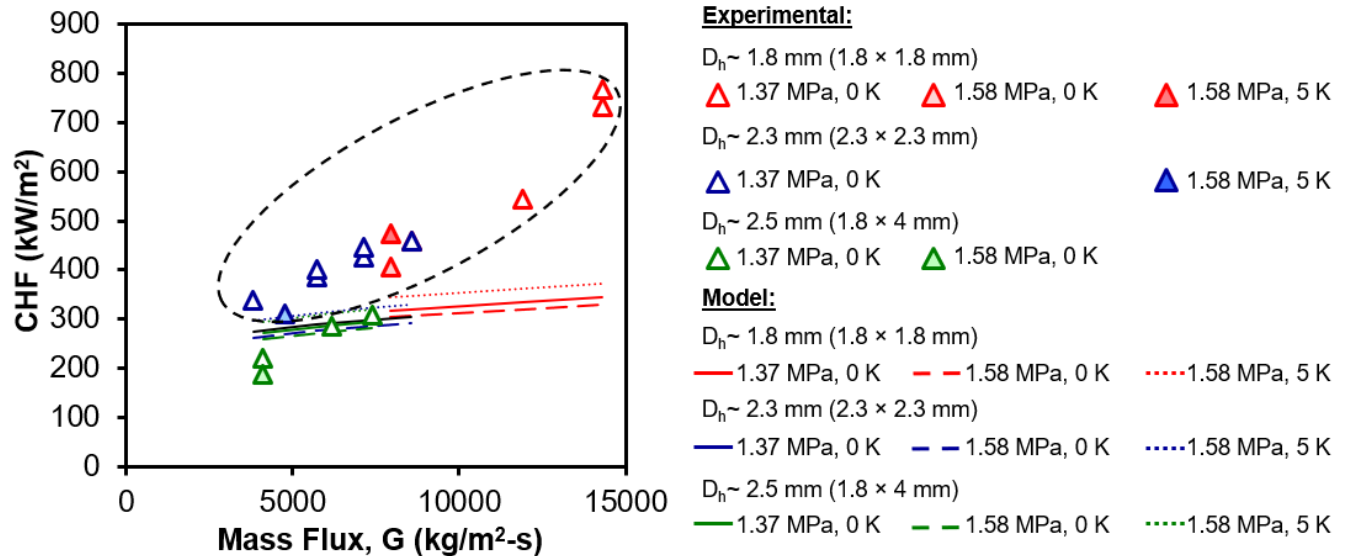


Figure 6-17. Model CHF values and Experimental CHF values as a function of mass flux under different operating conditions.

The expected MFBHF model values are shown in Figure 6-18 with the various flow rates, pressures, and subcooling degrees for all three samples; these values were obtained using Eqn. (6) through Eqn. (23). Comparing the models with the experimental values yielded an enhancement of 13 times greater values. That is a tremendous improvement for literature and the industry.

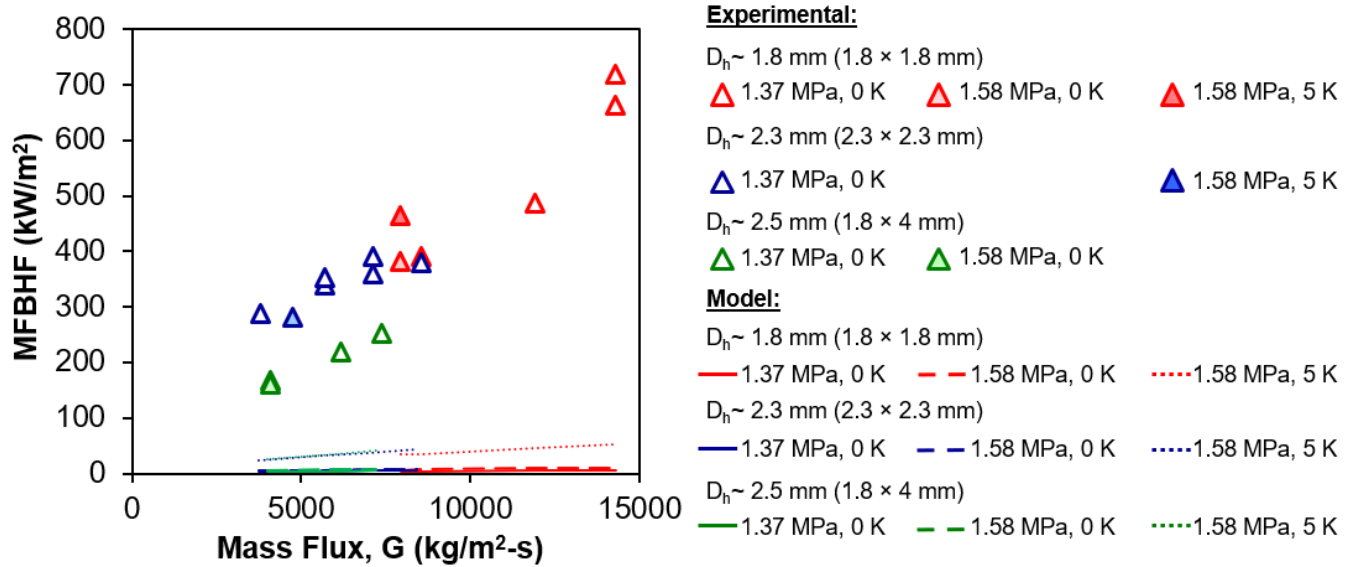


Figure 6-18. Model MFBHF values and Experimental MFBHF values as a function of mass flux under different operating conditions.

Chapter 7: Summary and Contributions

7.1 Overall Summary

The main objectives of this dissertation were defined as such:

1. To investigate the flow boiling heat transfer performance of additively manufactured cooling channels during asymmetric heating.
2. To identify the critical heat flux and minimum film boiling heat flux for various channels at various operating conditions.
3. To compare the experimental results with literature models to identify the heat transfer enhancement.

The motivation for this research is fueled by four major issues in the field of regenerative cooling of liquid rocket engines:

1. Most cooling channels being analyzed in the literature are typically conventionally manufactured, while the aerospace industry needs data with additively manufactured samples.
2. Surface roughness is not taken into account in the models.
3. Flow boiling experiments are performed with symmetrically heated cooling channels, even though rocket engines experience asymmetric heating.
4. Very little literature data is available for the minimum film boiling heat flux.

The single-phase forced convection study was conducted on four samples made from Inconel 625 with a hydraulic diameter of 3.2 mm (0.125”) with 4 different surface roughness values, INCO 0.8, INCO 3.2, INCO 6.4, and INCO 12.5. These samples were asymmetrically heated from the bottom with a heater block with steady heat flux. The results yielded that the sample with the highest surface roughness was the one with the highest Reynolds and Nusselt numbers. The NASA Rocketdyne correlation fit the results for the highest Reynolds and Nusselt numbers seen by INCO 12.5, but for the more average values for INCO 3.2 and INCO 6.3, the

Dittus-Boelter model and the Sieder-Tate model follow the trend. As for INCO 0.8, the lowest and most inefficient values, the Gnielinski correlation aligned better since it is more conservative and has lower Nusselt values. No correlation was able to fit for all samples under the various conditions.

Furthermore, the analysis of the forced convective boiling was conducted on three samples made from GRCo-42 with three hydraulic diameters, 1.8 mm (0.07"), 2.3 mm (0.09"), and 2.5 (0.097"). The operating conditions consisted of three different pressures, 0.89 MPa, 1.38 MPa, and 1.58 MPa (130 psi, 150 psi, 230 psi), three different volumetric flow rates, 31.5 cm³/s (0.5 gpm), 47.5 cm³/s (0.75 gpm), and 57 cm³/s (0.9 gpm), two subcooling degrees, 0 K and 5 K, and two working fluids, LN₂ and LCH₄. These samples were asymmetrically heated from the bottom with a heater block with changing steady state heat flux. The experimental results revealed that the sample with the highest critical heat flux and minimum film boiling heat flux values was the one with a hydraulic diameter of 1.8 mm (0.07"); CHF = 768 kW/m² with a mass flux of 14,295 kg/m²s; MFBHF = 719 kW/m² with a mass flux of 14,295 kg/m²s. It was determined that as the mass flux increases, so does the CHF and MFBHF.

In continuation with the forced convective boiling, pressure is inversely proportional to the latent heat of vaporization, as pressure rises, the latent energy decreases. And as pressure increases, the heat flux values decrease. The degree of subcooling was found to be a good mitigating factor; as the degree of subcooling grows, the heat flux increases, balancing the negative effects of higher pressures, which are inevitable in a rocket engine.

The results obtained for the forced convective boiling were compared to models in the literature, yielding to a 98% enhancement for the CHF and a 13 times greater enhancement for the MFBHF. More testing needs to be performed to obtain more MFBHF values.

7.2 Specific Contributions to the Field

The data provided in this investigation will contribute to the testing NASA Marshall Space Flight Center is conducting as they develop engines for the Artemis Program that plans on taking the first woman and more men to the moon. The heat transfer analysis also has the potential of contributing in several different cooling systems, as pool and flow boiling is a great source for cooling as the bubbles grow and depart from surfaces.

7.3 Recommendations for Future Research

Future research will be focused on a different cooling channel with an inside shape of a trapezoid to allow for faster bubble release and hopefully higher heat transfer capabilities. In addition, two other samples will be tested with microstructures inside the channel; one of the samples will have the shape running across the sample, while the other sample will have a pattern of structures that get repeated all across the channel.

Another proposition for the future would be to create a model that takes surface roughness into account and fits the results obtained herein.

References

- [1] Agostini, B., Revellin, R., Thome, J. R., Fabbri, M., Michel, B., Calmi, D., & Kloter, U. (2008). High heat flux flow boiling in silicon multi-microchannels–Part III: Saturated critical heat flux of R236fa and two-phase pressure drops. *International Journal of Heat and Mass Transfer*, 51(21-22), 5426-5442.
- [2] Akbar, M. K., Plummer, D. A., & Ghiaasiaan, S. M. (2002, January). Gas-liquid two-phase flow regimes in microchannels. In *ASME International Mechanical Engineering Congress and Exposition* (Vol. 3638, pp. 527-534).
- [3] An, T., Wang, Y., & Liu, W. Q. (2018). Experimental investigation of heat transfer characteristics of liquid nitrogen flow boiling in a mini-channel. In *International Heat Transfer Conference Digital Library*. Begel House Inc..
- [4] Back, L. H., Massier, P. F., & Gier, H. L. (1964). Convective heat transfer in a convergent-divergent nozzle. *International Journal of Heat and Mass Transfer*, 7(5), 549-568.
- [5] Balasubramanian, K., Jagirdar, M., Lee, P. S., Teo, C. J., & Chou, S. K. (2013). Experimental investigation of flow boiling heat transfer and instabilities in straight microchannels. *International journal of heat and mass transfer*, 66, 655-671.
- [6] Balasubramanian, K., Lee, P. S., Teo, C. J., & Chou, S. K. (2013). Flow boiling heat transfer and pressure drop in stepped fin microchannels. *International journal of heat and mass transfer*, 67, 234-252.
- [7] Bao, Z. Y., Fletcher, D. F., & Haynes, B. S. (2000). Flow boiling heat transfer of Freon R11 and HCFC123 in narrow passages. *International Journal of Heat and Mass Transfer*, 43(18), 3347-3358.
- [8] Bates, R. W., Maas, E. D., Irvine, S. A., Auyeung, T. P., & Perroomian, O. (2004). Design of a high heat flux facility for thermal stability testing of advanced hydrocarbon fuels. ENGINEERING RESEARCH AND CONSULTING INC HUNTSVILLE AL.
- [9] Bergles, A. E. (1962). Forced-convection surface-boiling heat transfer and burnout in tubes of small diameter (Doctoral dissertation, Massachusetts Institute of Technology).
- [10] Bertsch, S. S., Groll, E. A., & Garimella, S. V. (2009). A composite heat transfer correlation for saturated flow boiling in small channels. *International Journal of Heat and Mass Transfer*, 52(7-8), 2110-2118.
- [11] Bertsch, S. S., Groll, E. A., & Garimella, S. V. (2009). Effects of heat flux, mass flux, vapor quality, and saturation temperature on flow boiling heat transfer in microchannels. *International Journal of Multiphase Flow*, 35(2), 142-154.

- [12] Bogojevic, D., Sefiane, K., Duursma, G., & Walton, A. J. (2013). Bubble dynamics and flow boiling instabilities in microchannels. *International Journal of Heat and Mass Transfer*, 58(1-2), 663-675.
- [13] Brutin, D., Topin, F., & Tadrist, L. (2003). Experimental study of unsteady convective boiling in heated minichannels. *International Journal of Heat and Mass Transfer*, 46(16), 2957-2965.
- [14] Carey, V. P. (2020). *Liquid-vapor phase-change phenomena: an introduction to the thermophysics of vaporization and condensation processes in heat transfer equipment*. CRC Press.
- [15] Celata, G. P., Cumo, M., & Mariani, A. (1994). Assessment of correlations and models for the prediction of CHF in water subcooled flow boiling. *International journal of heat and mass transfer*, 37(2), 237-255.
- [16] Chen, A., Lin, T. F., Ali, H. M., & Yan, W. M. (2020). Experimental study on bubble characteristics of time periodic subcooled flow boiling in annular ducts due to wall heat flux oscillation. *International Journal of Heat and Mass Transfer*, 157, 119974.
- [17] Chen, S., Chen, X., Chen, L., Zhang, Q., & Hou, Y. (2019). Experimental study on the heat transfer characteristics of saturated liquid nitrogen flow boiling in small-diameter horizontal tubes. *Experimental Thermal and Fluid Science*, 101, 27-36.
- [18] Chen, T., & Garimella, S. V. (2006). Measurements and high-speed visualizations of flow boiling of a dielectric fluid in a silicon microchannel heat sink. *International Journal of Multiphase Flow*, 32(8), 957-971.
- [19] Chen, X., Chen, S., Chen, J., Li, J., Liu, X., Chen, L., & Hou, Y. (2017). Two-phase flow boiling frictional pressure drop of liquid nitrogen in horizontal circular mini-tubes: Experimental investigation and comparison with correlations. *Cryogenics*, 83, 85-94.
- [20] Cheng, L. (2013). Fundamental issues of critical heat flux phenomena during flow boiling in microscale-channels and nucleate pool boiling in confined spaces. *Heat transfer engineering*, 34(13), 1016-1043.
- [21] Darr, S. R., Hu, H., Shaeffer, R., Chung, J., Hartwig, J. W., & Majumdar, A. K. (2015). Numerical simulation of the liquid nitrogen chilldown of a vertical tube. In *53rd aiaa aerospace sciences meeting* (p. 0468).
- [22] Dittus, F. W., & Boelter, L. M. K. (1985). Heat transfer in automobile radiators of the tubular type. *International communications in heat and mass transfer*, 12(1), 3-22.
- [23] Doekhie, S., Dumont, E., Cervone, A., & Noomen, R. (2013). A computer-based tool for preliminary design and performance assessment of Continuous Detonation Wave Engines.

- [24] Fu, X., Qi, S. L., Zhang, P., & Wang, R. Z. (2008). Visualization of flow boiling of liquid nitrogen in a vertical mini-tube. *International journal of multiphase flow*, 34(4), 333-351.
- [25] Gong, M., Song, Q., Chen, G., Zhuang, X., Yang, Z., & Yao, Y. (2018). Boiling heat transfer characteristics for methane, ethane and their binary mixtures. *Heat Transfer Engineering*.
- [26] Gradl, P. R., Protz, C. S., & Wammen, T. (2019). Additive manufacturing and hot-fire testing of liquid rocket channel wall nozzles using blown powder directed energy deposition inconel 625 and JBK-75 Alloys. In *AIAA Propulsion and Energy 2019 Forum* (p. 4362).
- [27] Gradl, P. R., Protz, C. S., Cooper, K., Ellis, D., Evans, L. J., & Garcia, C. (2019). GRCop-42 development and hot-fire testing using additive manufacturing powder bed fusion for channel-cooled combustion chambers. In *AIAA Propulsion and Energy 2019 Forum* (p. 4228).
- [28] Groeneveld, D. C., Cheng, S. C., & Doan, T. (1986). 1986 AECL-UO critical heat flux lookup table. *Heat transfer engineering*, 7(1-2), 46-62.
- [29] Haemisch, J., Suslov, D., & Oschwald, M. (2019). Experimental study of methane heat transfer deterioration in a subscale combustion chamber. *Journal of Propulsion and Power*, 35(4), 819-826.
- [30] Hartwig, J., Hu, H., Styborski, J., & Chung, J. N. (2015). Comparison of cryogenic flow boiling in liquid nitrogen and liquid hydrogen chilldown experiments. *International Journal of Heat and Mass Transfer*, 88, 662-673.
- [31] Hernandez, L., Palacios, R., Ortega, D., Adams, J., Bugarin, L. I., Rahman, M. M., & Choudhuri, A. R. (2019). The Effect of Surface Roughness on LCH₄ Boiling Heat Transfer Performance of Conventionally and Additively Manufactured Rocket Engine Regenerative Cooling Channels. In *AIAA Propulsion and Energy 2019 Forum* (p. 4363).
- [32] Hernandez, Linda E. "The Effect of Surface Roughness on LCH₄ Boiling Heat Transfer Performance of Conventionally and Additively Manufactured Rocket Engine Regenerative Cooling Channels." The University of Texas at El Paso, 2019.
- [33] Irvine, S. A., & Burns, R. M. (2005). Preliminary Heat Transfer Characteristics of RP-2 Fuel as Tested in the High Heat Flux Facility (PREPRINT). AIR FORCE RESEARCH LAB EDWARDS AFB CA PROPULSION DIRECTORATE.
- [34] Jones, R. C., & Judd, R. L. (2003). An investigation of dryout/rewetting in subcooled two-phase flow boiling. *International journal of heat and mass transfer*, 46(17), 3143-3152.

- [35] Kandlikar, S. G., & Grande, W. J. (2003). Evolution of microchannel flow passages-- thermohydraulic performance and fabrication technology. *Heat transfer engineering*, 24(1), 3-17.
- [36] Kandlikar, S. G., Joshi, S., & Tian, S. (2003). Effect of surface roughness on heat transfer and fluid flow characteristics at low Reynolds numbers in small diameter tubes. *Heat Transfer Engineering*, 24(3), 4-16.
- [37] Kandlikar, S. G., & Steinke, M. E. (2002). Flow Boiling Heat Transfer Coefficient In Minichannels– Correlation and Trends. In *International Heat Transfer Conference Digital Library*. Begel House Inc..
- [38] Kandlikar, S. G. (1990). A general correlation for saturated two-phase flow boiling heat transfer inside horizontal and vertical tubes.
- [39] Kandlikar, S. G. (2001). Fundamental issues related to flow boiling in minichannels and microchannels. *Proc. Experimental Heat Transfer, Fluid Mechanics and Thermodynamics*, Thessaloniki, 129-146.
- [40] Kandlikar, S. G. (2004). Heat transfer mechanisms during flow boiling in microchannels. *J. Heat Transfer*, 126(1), 8-16.
- [41] Katto, Y. (1981). General features of CHF of forced convection boiling in uniformly heated rectangular channels. *International Journal of Heat and Mass Transfer*, 24(8), 1413-1419.
- [42] Katto, Y. (1978). A generalized correlation of critical heat flux for the forced convection boiling in vertical uniformly heated round tubes. *International Journal of Heat and Mass Transfer*, 21(12), 1527-1542.
- [43] Katto, Y. (1980). General features of CHF of forced convection boiling in uniformly heated vertical tubes with zero inlet subcooling. *International Journal of Heat and Mass Transfer*, 23(4), 493-504.
- [44] Katto, Y. (1980). Critical heat flux of forced convection boiling in uniformly heated vertical tubes (correlation of CHF in HP-regime and determination of CHF-regime map). *International Journal of Heat and Mass Transfer*, 23(11), 1573-1580.
- [45] Katto, Y., & Ohno, H. (1984). An improved version of the generalized correlation of critical heat flux for the forced convective boiling in uniformly heated vertical tubes. *International journal of heat and mass transfer*, 27(9), 1641-1648.
- [46] Kennedy, J. E., Roach Jr, G. M., Dowling, M. F., Abdel-Khalik, S. I., Ghiaasiaan, S. M., Jeter, S. M., & Quershi, Z. H. (2000). The onset of flow instability in uniformly heated horizontal microchannels. *J. Heat Transfer*, 122(1), 118-125.
- [47] Kharangate, C. R., O'Neill, L. E., & Mudawar, I. (2016). Effects of two-phase inlet quality, mass velocity, flow orientation, and heating perimeter on flow boiling in a

rectangular channel: Part 1—Two-phase flow and heat transfer results. *International journal of heat and mass transfer*, 103, 1261-1279.

- [48] Kharangate, C. R., O'Neill, L. E., & Mudawar, I. (2016). Effects of two-phase inlet quality, mass velocity, flow orientation, and heating perimeter on flow boiling in a rectangular channel: Part 2—CHF experimental results and model. *International journal of heat and mass transfer*, 103, 1280-1296.
- [49] Kim, S. M., & Mudawar, I. (2013). Universal approach to predicting saturated flow boiling heat transfer in mini/micro-channels—Part I. Dryout incipience quality. *International Journal of Heat and Mass Transfer*, 64, 1226-1238.
- [50] Kim, S. M., & Mudawar, I. (2013). Universal approach to predicting two-phase frictional pressure drop for mini/micro-channel saturated flow boiling. *International Journal of Heat and Mass Transfer*, 58(1-2), 718-734.
- [51] Klimenko, V. V. (1982). Heat transfer intensity at forced flow boiling of cryogenic liquids in tubes. *Cryogenics*, 22(11), 569-576.
- [52] Kudo, Y., Nakaiso, K., Kariya, K., & Miyara, A. (2016). Experimental study on boiling and condensation heat transfer in a horizontal mini channel.
- [53] Lazarek, G. M., & Black, S. H. (1982). Evaporative heat transfer, pressure drop and critical heat flux in a small vertical tube with R-113. *International Journal of Heat and Mass Transfer*, 25(7), 945-960.
- [54] Lee, H. J., & Lee, S. Y. (2001). Heat transfer correlation for boiling flows in small rectangular horizontal channels with low aspect ratios. *International Journal of Multiphase Flow*, 27(12), 2043-2062.
- [55] Lee, J. Y., Kim, M. H., Kaviany, M., & Son, S. Y. (2011). Bubble nucleation in microchannel flow boiling using single artificial cavity. *International journal of heat and mass transfer*, 54(25-26), 5139-5148.
- [56] Lee, J., & Mudawar, I. (2005). Two-phase flow in high-heat-flux micro-channel heat sink for refrigeration cooling applications: Part II—heat transfer characteristics. *International Journal of Heat and Mass Transfer*, 48(5), 941-955.
- [57] Lee, J., & Mudawar, I. (2005). Two-phase flow in high-heat-flux micro-channel heat sink for refrigeration cooling applications: Part I—pressure drop characteristics. *International Journal of Heat and Mass Transfer*, 48(5), 928-940.
- [58] Lee, J., & Mudawar, I. (2008). Fluid flow and heat transfer characteristics of low temperature two-phase micro-channel heat sinks—Part 1: Experimental methods and flow visualization results. *International Journal of Heat and Mass Transfer*, 51(17-18), 4315-4326.






- [59] Lee, S., Devahdhanush, V. S., & Mudawar, I. (2018). Investigation of subcooled and saturated boiling heat transfer mechanisms, instabilities, and transient flow regime maps for large length-to-diameter ratio micro-channel heat sinks. *International Journal of Heat and Mass Transfer*, 123, 172-191.
- [60] Lee, S., & Mudawar, I. (2019). Enhanced model for annular flow in micro-channel heat sinks, including effects of droplet entrainment/deposition and core turbulence. *International Journal of Heat and Mass Transfer*, 133, 510-530.
- [61] Li, Y., Xia, G., Jia, Y., Cheng, Y., & Wang, J. (2017). Experimental investigation of flow boiling performance in microchannels with and without triangular cavities—a comparative study. *International Journal of Heat and Mass Transfer*, 108, 1511-1526.
- [62] Liu, D., Lee, P. S., & Garimella, S. V. (2005). Prediction of the onset of nucleate boiling in microchannel flow. *International Journal of Heat and Mass Transfer*, 48(25-26), 5134-5149.
- [63] Liu, X., Chen, X., Zhang, Q., Wang, S., Hou, Y., & Chen, L. (2017). Investigation on CHF of saturated liquid nitrogen flow boiling in a horizontal small channel. *Applied Thermal Engineering*, 125, 1025-1036.
- [64] Liu, Y., Liu, W., Gu, L., Shan, J., Zhang, L., & Su, X. (2022). Existing DNB-type CHF mechanistic models and relations with visualized experiments in forced convective flow boiling: A review. *Progress in Nuclear Energy*, 148, 104225.
- [65] Lochrie, A. J. (1955). The effect of acoustic vibrations on the heat transfer coefficient in a closed air chamber (Doctoral dissertation, Georgia Institute of Technology).
- [66] Maas, E., Irvine, S., Bates, R., & Auyeung, T. (2005). A high heat flux facility design for testing of advanced hydrocarbon fuel thermal stability. In 43rd AIAA Aerospace Sciences Meeting and Exhibit (p. 363).
- [67] Mehendale, S. S., Jacobi, A. M., and Shah, R. K., *Fluid Flow and Heat Transfer at Micro- and Meso-Scales with Applications to Heat Exchanger Design*, Applied Mechanics Review, vol. 53, pp. 175–193, 2000.
- [68] Mills, A. F. (1992). *Heat transfer*. CRC Press.
- [69] Mishima, K., & Hibiki, T. (1996). Some characteristics of air-water two-phase flow in small diameter vertical tubes. *International journal of multiphase flow*, 22(4), 703-712.
- [70] Ong, C. L., & Thome, J. R. (2011). Macro-to-microchannel transition in two-phase flow: Part 2—Flow boiling heat transfer and critical heat flux. *Experimental thermal and fluid science*, 35(6), 873-886.

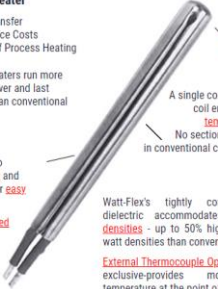
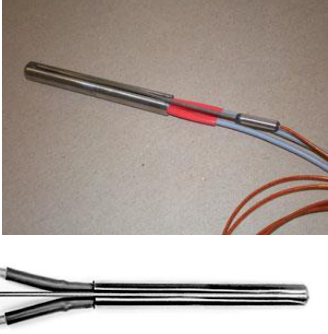



- [71] Ong, C. L., & Thome, J. R. (2011). Macro-to-microchannel transition in two-phase flow: Part 1—Two-phase flow patterns and film thickness measurements. *Experimental Thermal and Fluid Science*, 35(1), 37-47.
- [72] Ortega, D., Palacios, R. E., Olvera, G., Hernandez, L., Adams, J. R., Rahman, M. M., & Choudhuri, A. R. (2020). Roughness Augmented High Pressure Flow Boiling Heat Transfer Enhancement using LN2 and LCH4 on Additively Manufactured Rocket Engine Regenerative Cooling Channels. In *AIAA Propulsion and Energy 2020 Forum* (p. 3942).
- [73] Prajapati, Y. K., & Bhandari, P. (2017). Flow boiling instabilities in microchannels and their promising solutions—A review. *Experimental Thermal and Fluid Science*, 88, 576-593.
- [74] Prajapati, Y. K., & Bhandari, P. (2017). Flow boiling instabilities in microchannels and their promising solutions—A review. *Experimental Thermal and Fluid Science*, 88, 576-593.
- [75] Qi, S. L., Zhang, P., Wang, R. Z., & Xu, L. X. (2007). Flow boiling of liquid nitrogen in micro-tubes: Part II—Heat transfer characteristics and critical heat flux. *International journal of heat and mass transfer*, 50(25-26), 5017-5030.
- [76] Qi, S. L., Zhang, P., Wang, R. Z., & Xu, L. X. (2007). Flow boiling of liquid nitrogen in micro-tubes: Part I—The onset of nucleate boiling, two-phase flow instability and two-phase flow pressure drop. *International journal of heat and mass transfer*, 50(25-26), 4999-5016.
- [77] Rocket Propulsion Basics. Rocket Propulsion - Basic Principles, <https://www.mpoweruk.com/rockets.htm>
- [78] Saitoh, S., Daiguji, H., & Hihara, E. (2005). Effect of tube diameter on boiling heat transfer of R-134a in horizontal small-diameter tubes. *International Journal of Heat and Mass Transfer*, 48(23-24), 4973-4984.
- [79] Sandoval, A., Gutierrez, E., Chaparro, J., Bugarin, L., Adams, J., Choudhuri, A. R., & Melcher, J. (2018). Experimental Investigation of LN2 Convection and Boiling in Traditionally and Additively Manufactured Rocket Engine Cooling Channels. In *2018 International Energy Conversion Engineering Conference* (p. 4698).
- [80] Selwood, J. L. B. (1949). Some Observations on the Problems of Rocket-Motor Cooling Design. *Journal of the American Rocket Society*, (76), 16-26.
- [81] Simon, F. F., Papell, S. S., & Simoneau, R. J. (1968). Minimum film-boiling heat flux in vertical flow of liquid nitrogen. National Aeronautics and Space Administration.
- [82] Suo, M., & Griffith, P. (1964). Two-phase flow in capillary tubes.





- [83] Tibirica, C. B., & Ribatski, G. (2013). Flow boiling in micro-scale channels—Synthesized literature review. *International Journal of Refrigeration*, 36(2), 301-324.
- [84] Tibiriçá, C. B., & Ribatski, G. (2014). Flow patterns and bubble departure fundamental characteristics during flow boiling in microscale channels. *Experimental Thermal and Fluid Science*, 59, 152-165.
- [85] Trejo, A., Garcia, C., & Choudhuri, A. (2016). Experimental investigation of transient forced convection of liquid methane in a channel at high heat flux conditions. *Experimental Heat Transfer*, 29(1), 97-112.
- [86] Trejo, A., Trujillo, A., Galvan, M., Choudhuri, A., Melcher, J. C., & Bruggemann, J. J. (2016). Experimental investigation of methane convection and boiling in rocket engine cooling channels. *Journal of Thermophysics and Heat Transfer*, 30(4), 937-945.
- [87] VanNoord, J. (2010, November). A Heat Transfer Investigation of Liquid and Two-Phase Methane. In *57th Joint Army-Navy-NASA-Air Force (JANNAF) Propulsion Meeting* (No. E-17494).
- [88] Wafer, W. J. (1971). The effect of diameter on the film boiling behavior of liquid nitrogen.
- [89] Zhang, B. C., Li, Q. L., Wang, Y., Zhang, J. Q., Song, J., & Zhuang, F. C. (2020). Experimental investigation of nitrogen flow boiling heat transfer in a single mini-channel. *Journal of Zhejiang University-SCIENCE A*, 21(2), 147-166.
- [90] Zhang, H., & Hewitt, G. F. (2016). Phenomenological modelling of CHF in annular flow in annuli using new models of droplet deposition and entrainment. *Nuclear Engineering and Design*, 305, 284-292.

Appendix A – Instrumentation

TABLE A-1. HIGH HEAT FLUX TESTING FACILITY INSTRUMENTATION

Component	Manufacturer	Model	Picture	Range
Cryogenic Pressure Transducer	Omega Engineering	PX1005L-500AV		0 to 3.45 MPa (0 to 500 psia)
Static Pressure Transducer	Spectre Corp	Model 1000-A		0 to 3.45 MPa (0 to 500 psia) Error: 0.5% & 0.2% BFSL (Standard)
Quick Disconnect 0.125" OD, 6", Exposed Tip Type E Thermocouple	Omega Engineering	EMQSS-125E-6		-200 to 900°C (-328 to 1652°F) Error °C: 1.7°C or 0.5% above 0°C
Quick Disconnect 0.040" OD, 6" Exposed Tip Type E Thermocouple	Omega Engineering	EMQSS-040E-6		-200 to 900°C (-328 to 1652°F) Error °C: 1.7°C or 0.5% above 0°C
Quick Disconnect 0.125" OD, 6", Exposed Tip Type K Thermocouple	Omega Engineering	KMQSS-125E-6		-200 to 1250°C (-328 to 2282°F) Error °C: 2.2°C or 0.75% above 0°C

<p>Watt-Flex Cartridge Heater 0.25"x6.5", 450 W, with side groove</p>	<p>Dalton Electric</p>	<p>HDC00084</p>	<p>Watt-Flex Cartridge Heaters The Revolutionary Watt-Flex® Split-Sheath Cartridge Heater</p> <ul style="list-style-type: none"> • Maximizes Heat Transfer • Reduces Maintenance Costs • Reduces the Cost of Process Heating <p>Watt-Flex Cartridge Heaters run more efficiently, use less power and last up to 5 times longer than conventional cartridge heaters.</p> <p>Split-sheath expands to maximize heat transfer and contracts when cold for easy removal from bore.</p> <p>Ideal for use in oversized bores. Eliminates need for tight fits, tight tolerance bores.</p>  <p>Hot Tip or Cool Tip Option</p> <p>A single continuous heating coil ensures a uniform temperature profile. No sections to burn out as in conventional cartridge heaters.</p> <p>Watt-Flex's tightly compacted MgO dielectric accommodates higher watt densities - up to 50% higher warrantable watt densities than conventional heaters.</p> <p>External Thermocouple Option - a Watt-Flex exclusive provides more accurate temperature at the point of heat transfer to host metal.</p> <p>en Español, marquis aquí Resistencias de cartucho Watt-Flex</p>	
<p>0.040" OD, 8" Type K Thermocouple (Goes inside groove of cartridge heater)</p>	<p>Dalton Electric</p>	<p>TC-KG40D080L012</p>		<p>-200 to 1250°C (-328 to 2282°F) Error °C: 2.2°C or 0.75% above 0°C</p>
<p>Scroll Vacuum Pump</p>	<p>BOC Edwards</p>	<p>XDS5</p>		
<p>Convection-Enhanced Pirani Sensor</p>	<p>Kurt J. Lesker</p>	<p>K31714S</p>		<p>1x10⁻³ to 1x10³ Torr (1.9 x 10⁻⁵ to 19 psi) Error: ±<1%</p>
<p>Digital Convection Pirani Vacuum Gauge Controller</p>	<p>MKS</p>	<p>HPS 947</p>		<p>1x10⁻³ to 1x10³ Torr (1.9 x 10⁻⁵ to 19 psi) Error: ±<1%</p>

Terminal block with SCC Expansion Slots DAQ Device	National Instruments	NI cDAQ-9174		Refer to Manual
Thermocouple Input Module DAQ Device	National Instruments	NI-9213		Refer to Manual
Analog Input C Series Module	National Instruments	NI-9205		Refer to Manual
Pressure Transducer Process Meter and Controller (Amplifier)	Omega Engineering	DP25B-E-A		0 to 100 mV Error %: $\pm 0.02\%$ of reading

Appendix B – Extra Data

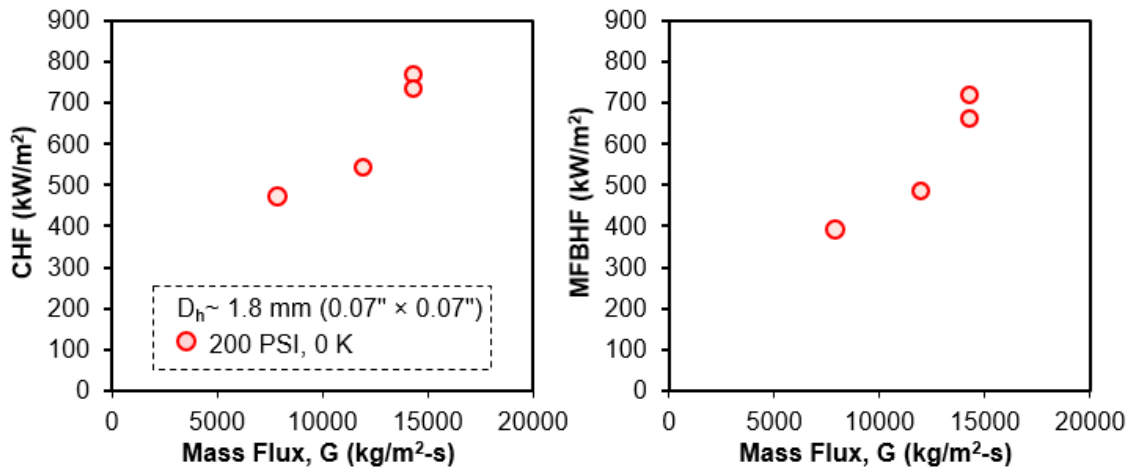


Figure B-1. CHF and MFBHF for sample with $D_h = 1.8$ mm as a function of mass flux

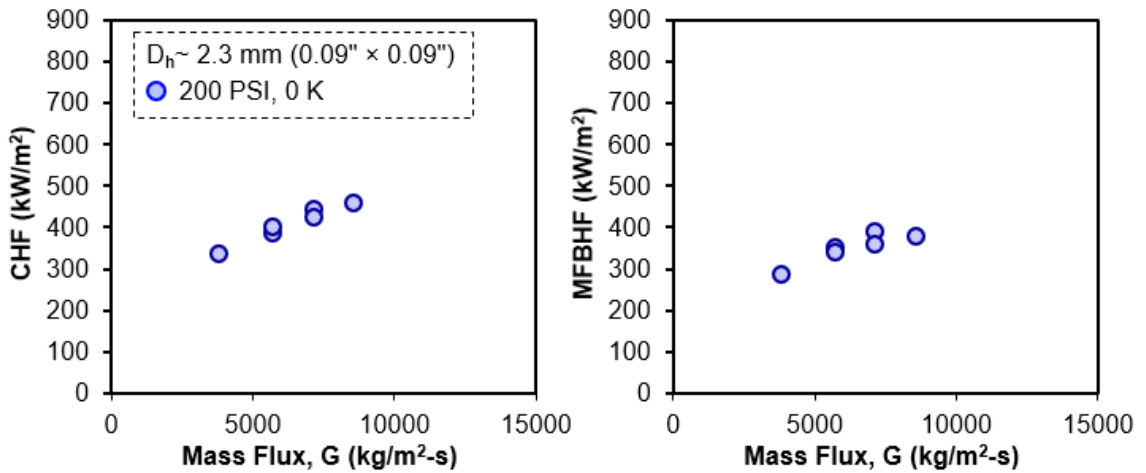


Figure B-2. CHF and MFBHF for sample with $D_h = 2.3$ mm as a function of mass flux

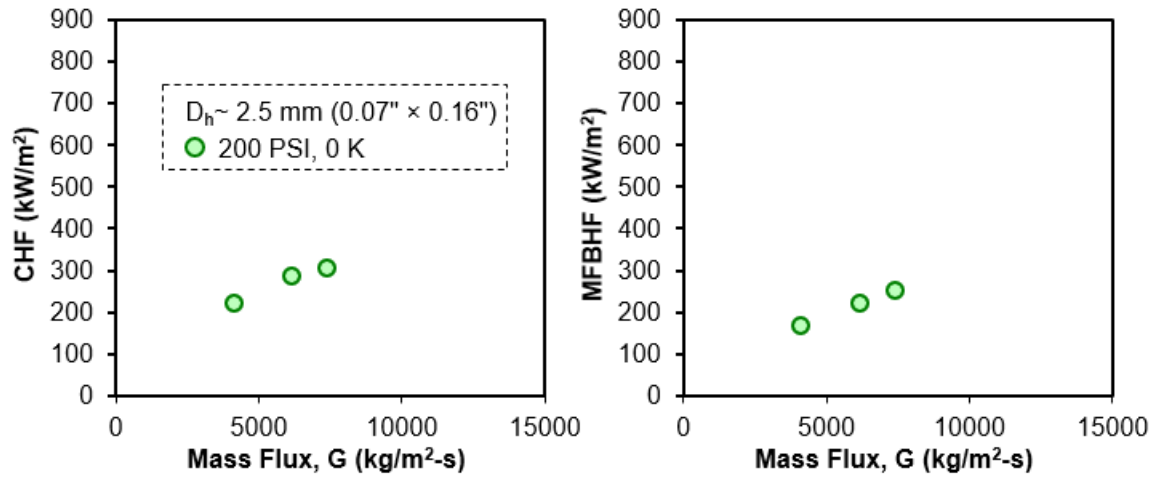


Figure B-3. CHF and MFBHF for sample with $D_h = 2.5$ mm as a function of mass flux

Curriculum Vita

Debra Jazmin Ortega was born on January 11, 1993, in a small town, Andrews, Texas. She attended elementary school in Cd. Juarez, Chih., Mexico. She completed her high school at Bowie High School and earned a Bachelor of Science in Mechanical Engineering from The University of Texas at El Paso (UTEP). She started her Ph.D. in 2018 at UTEP and joined the Aerospace Center as a Ph.D. Research Assistant. While part of the Center, she became part of the High Heat Flux Testing Facility (HHFTF) team, and after two years, she became team lead and continued testing under a National Aeronautics and Space Administration (NASA) Marshall Space Flight Center grant. The project focused on enhancing heat transfer in the cooling channels of a rocket engine which became her Ph.D. research topic. In addition, Debra assisted in the test operations for a 500 lbf liquid oxygen/methane engine (CROME) and supported the Lunar Surface Technology Research team in ice collection and liquid nitrogen evaporation testing for a prototype for water mining on the surface of the moon. Prior to completing her degree, she completed a Graduate Certificate in 3D Engineering and Additive Manufacturing. She was also hired by NASA Marshall Space Flight Center for the Pathways Internship, where she completed two rotations. The first rotation took place with the Structural and Mechanical Design Branch, where she characterized an air bearing's plenum for constant pressure output and designed a system to mitigate debris from damaging the Flight Robotics Lab's Flat Floor to reduce repairment costs. During her second rotation, she joined the Engine Systems Branch, where she processed RS-25 single-engine testing by analyzing trending data for anomalies to develop the next generation of SLS core stage engines. Debra is a contributing author for several conference papers and published several others as the principal author for JPC, SETS, ASCEND, IMECE, and Sci-Tech. After completing her degree, Debra will join Blue Origin as a Test Engineer in West Texas Launch Site One at VEEEx.